

Ferritin encapsulated PbS, PbSe, and MoS₂ Nanocrystals for Photovoltaic Applications

Kameron Rex Hansen

A senior thesis submitted to the faculty of
Brigham Young University
in partial fulfillment of the requirements for the degree of

Bachelor of Science

John Colton, Advisor

Department of Physics and Astronomy

Brigham Young University

April 2017

Copyright © 2017 Kameron Rex Hansen

All Rights Reserved

ABSTRACT

Ferritin encapsulated PbS, PbSe, and MoS₂ Nanocrystals for Photovoltaic Applications

Kameron Rex Hansen
Department of Physics and Astronomy, BYU
Bachelor of Science

This thesis presents a new synthesis method for PbSe and MoS₂ semiconductor nanoparticles inside the protein ferritin. It also presents a simplified synthesis method for PbS, based on the work of Hennequin, et al [1]. To our knowledge, PbSe and MoS₂ nanoparticles have not been synthesized inside ferritin before. All three materials could potentially have several applications outside photovoltaics, e.g. as biological markers and cancer therapies; however, this thesis focuses on their application to photovoltaics. PbS-ferritin is used to replace dye molecules in a dye-sensitized solar cell and the device shows an efficiency of 0.28%.

Keywords: lead sulfide, lead selenide, ferritin, photovoltaic

ACKNOWLEDGMENTS

Thank you to Shawn Cornally and Bennett Brown for taking genuine interest in each student and inspiring my curiosity towards physics. I would like to dedicate this thesis to Dr. John Colton for the countless hours he has spent mentoring all of the lab members; without his talent for clearly explaining complex concepts, my understanding of real world applications of physics would be far more limited. I would like to thank Richard Watt for continually sharing his expertise and resources to support this project. The acquisition of this thesis's data would not have been possible without the help of my undergraduate classmates: Cameron Olsen, Ryan Peterson, Alessandro Perego, Heather Hogg, Luis Perez, and Andrew Henrichsen. Lastly, I would like to thank my parents, siblings, and my wife Madeline Brenchley for supporting me.

Contents

Table of Contents	iv
List of Figures	1
1 Introduction	2
1.1 Overview of Thesis	2
1.1.1 Significance	2
1.1.2 Summary of Presented Work	3
1.2 Ferritin with Native Cores	4
1.3 Ferritin with Non-native Cores	5
1.3.1 Applications	6
1.3.2 Synthesis Strategies	6
1.4 Quantum Dots	7
1.5 The Dye Sensitized Solar Cell	8
2 Experimental Methods	12
2.1 Apoferritin Preparation	12
2.2 PbS-FTN and PbSe-FTN Synthesis	13
2.3 MoS ₂ -FTN Synthesis	14
2.4 Gel-Filtration Chromatography	15
2.5 Protein Quantification	15
2.6 Metal Quantification	17
2.7 TEM analysis	17
2.8 Photoluminescence	17
2.9 Solar cell fabrication	18
2.10 IV measurements	19
3 Synthesis Results and Discussion	21
3.1 PbS-FTN	21
3.2 PbSe-FTN	25
3.3 MoS ₂ -FTN	27

4	Optical Characterization: Results and Discussion	29
4.1	Photoluminescence	29
4.2	Photocorrosion: PbS vs PbS-FTN	30
4.3	IV Performance	32
5	Conclusions	35
5.1	Summary	35
5.2	Future work	36
5.2.1	Micro-PL and Micro-photocurrent Experiments	36
5.2.2	Crystalline Ferritin Device	37
	Appendix A Appendix: Watt Lab Experimental Procedures	39
A.1	Apoferritin Preparation	40
A.2	Gel Filtration	43
A.2.1	Making the column	43
A.2.2	Running the column	44
A.3	ICP-MS Sample Preparation	46
A.3.1	Materials	46
A.3.2	Procedure	47
A.4	TEM Sample Preparation	49
A.4.1	Materials	50
A.4.2	Procedure	50
A.5	Inert Atmospheres	52
A.5.1	Glove Box	53
A.5.2	Vacuum-Gas Manifold System	53
	Bibliography	55

List of Figures

1.1	The Ferritin Protein Structure	4
1.2	Dye Sensitized Solar Cell Mechanism	9
2.1	Solar Cell Fabrication	18
3.1	Table of PbS-FTN Synthesis Results	22
3.2	PbS-FTN Aerobic vs Anaerobic Synthesis	23
3.3	TEM images of PbS-FTN	24
3.4	Table of PbSe-FTN Synthesis Results	26
3.5	PbSe-FTN Absorbance by Fraction	26
3.6	TEM images of PbSe-FTN and MoS ₂ -FTN	27
3.7	MoS ₂ -FTN Metal/Protein Concentrations by Fraction	28
4.1	PbS-FTN Photoluminescence	30
4.2	Photocorrosion: PbS vs PbS-FTN	31
4.3	Time Evolution of Photoluminescence: PbS vs PbS-FTN	31
4.4	IV measurements	33
A.1	Apoferritin Dialysis	41
A.2	Gravity Column	43

A.3	ICP-MS Materials	46
A.4	Staining Copper Grid	49
A.5	Vacuum-Gas Manifold System	52

Chapter 1

Introduction

1.1 Overview of Thesis

1.1.1 Significance

The materials studied in this thesis, lead sulfide inside ferritin (PbS-FTN), lead selenide inside ferritin (PbSe-FTN) and MoS₂ inside ferritin (MoS₂-FTN), could potentially have several applications outside photovoltaics, e.g. as biological markers [2] and cancer therapies [3]; however, this thesis focuses on their application to photovoltaics. Solar energy is considered by many to be the renewable energy source most capable of becoming economically competitive with fossil fuels. Once a nontoxic, cheap, stable, and high efficiency device is realized, economies of scale can lower manufacturing prices and potentially reach the Department of Energy's goal for \$1/W solar systems [4].

Currently, there are many technologies that appear more promising than dye sensitized solar cells. Monocrystalline silicon solar cells have reached grid parity in 20 US states [5], while perovskite and thin-film devices have surpassed 20 percent efficiency and sparked the birth of several start-ups [6]. Yet these technologies are not without flaws: manufacturing of monocrystalline sili-

con wafers is expensive, perovskites are unstable and contain toxic lead ions, and CdTe thin-films rely on rare materials. For these reasons, we believe solutions that involve radically different materials are still worthy of pursuit, such as the materials this thesis investigates: PbS-FTN, PbSe-FTN¹, and MoS₂.

1.1.2 Summary of Presented Work

We hypothesize that the toxicity, instability [8], and clustering [9] issues of PbS and PbSe quantum dots, which otherwise show a high potential as photon-absorbers in dye sensitized solar cells, can be solved by encapsulating the quantum dots in the protein ferritin. The foundation for this hypothesis lies in several experiments that demonstrate ferritin's biocompatibility [7], thermal and chemical stability [10], its ability to serve as a template for even, uniform nanocrystal growth [11, 12], and its ability to be arranged in ordered arrays [13]. Yet, it is possible the ferritin presents too high of an electron tunneling barrier for these materials to be effective in a photovoltaic system. To begin testing this hypothesis, we fabricate and characterize dye sensitized solar cells with PbS-FTN as the dye.

A separate focus of this thesis is the synthesis of PbS-FTN, PbSe-FTN and MoS₂-FTN. We simplify Hennequin's synthesis of PbS-FTN [1] by demonstrating it can be carried out under an oxygen atmosphere and does not require a Pb:S ratio of 1:0.3; we instead use a 1:1 ratio. We introduce the synthesis of PbSe-FTN which is achieved by replacing the Na₂S with Na₂Se in Hennequin's PbS-FTN synthesis. Lastly, we introduce a recombination synthesis method for MoS₂-FTN.

¹Studies suggest the lead in PbS-FTN and PbSe-FTN is not toxic because it is confined within ferritin [7].

1.2 Ferritin with Native Cores

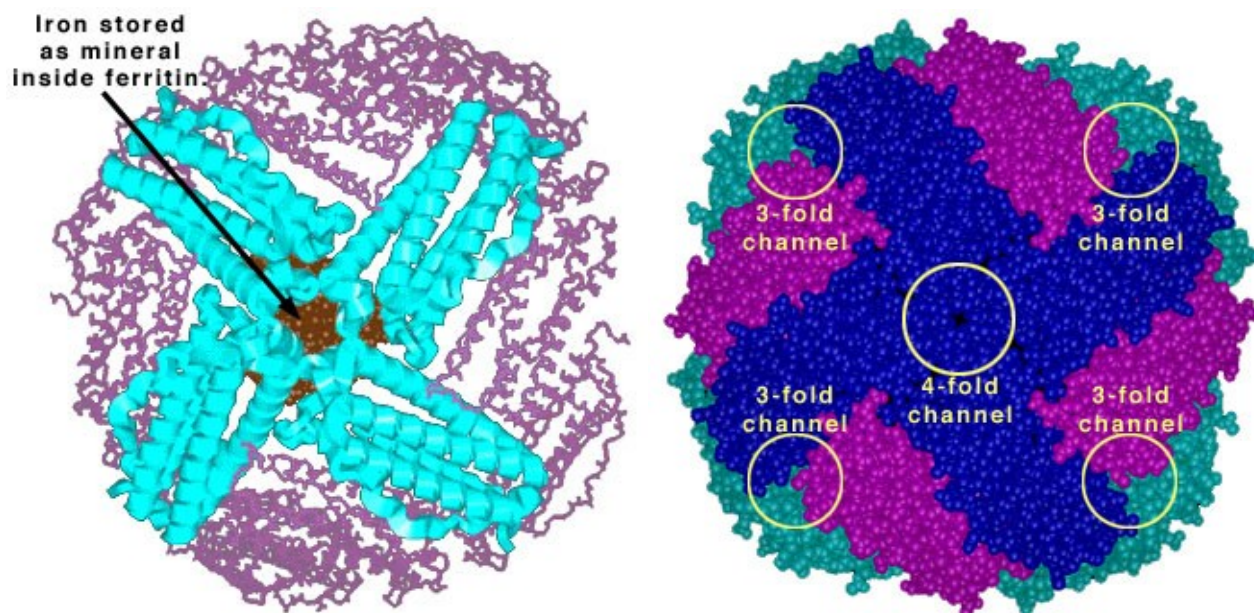


Figure 1.1 (Left) The protein ferritin is a spherical shell that, in its natural state, houses an iron oxide mineral. (Right) CPK representation of ferritin showing the 3-fold and 4-fold ion channels. In the CPK representation, each atom is represented by a dot with radius equal to the atom's van der Waals radius. Both figures were acquired with permission from Washington University in St. Louis [14].

A protein is a combination of amino acids that fold together into structures, which biologist classify into four levels of complexity: primary (amino acid chains), secondary (folding of amino acid chains into a sheet or helix), tertiary (sub-unit of a protein), and quaternary (the full protein). The function of any given protein is uniquely determined by the three-dimensional shape of its quaternary structure.

Ferritin is a spherical protein shell (8 nm inner diameter, 12 nm outer diameter) that is universally used by life to store iron. A storage unit for iron is necessary because the production of hemoglobin (used to transport oxygen) requires iron, and free iron ions are toxic at high concentration. Compared to other proteins, ferritin is extremely thermally and chemically stable. It is able to maintain its quaternary form up to 70° C and within a pH range of 3.4 - 10 [10, 15].

The quaternary structure of ferritin is composed of peptide subunits which come in two varieties: H-chain and L-chain. The H and L refer to the subunit's respective molecular weight, H for heavy (21 kDa) and L for light (19 kDa). A complete ferritin protein always has 24 subunits (450-474 kDa), however the ratio between H-chain and L-chain subunits varies depending on the organism and even the location within the organism [16].

The H-chain and L-chain subunits fold together in a manner that creates channels with threefold and fourfold symmetry [17]. The channels connect the cavity to the outside and provide permeation pathways for ions and protons. As determined by X-ray crystallography measurements, these channels are similar in size but have different electrostatic properties—it's the electrostatic properties that define the channel's role in iron uptake and release: positive Fe^{2+} ions enter the negative threefold channel and exit the positive fourfold channel [17].

After entering the threefold channel, Fe^{2+} ions are held in a unique ferroxidase center and are oxidized to Fe^{3+} by oxygen. The ferroxidase center can hold two Fe^{2+} ions and its structure catalyzes the oxidation to Fe^{3+} , which is necessary to form $\text{Fe}(\text{O})\text{OH}$, the natural occurring "ferrihydrite" mineral. After oxidation, Fe^{3+} ions migrate to the interior side of the L-chain subunit to form $\text{Fe}(\text{O})\text{OH}$. As more Fe^{3+} enters the cavity, the $\text{Fe}(\text{O})\text{OH}$ mineral grows inwards from H-sites on the interior surface of the cavity. Thus, a complete spherical core is not formed until until these separate hemisphere-shaped minerals grow large enough to connect in the center [18, 19].

1.3 Ferritin with Non-native Cores

The native ferrihydrite mineral $\text{Fe}(\text{O})\text{OH}$ stored inside ferritin can be removed and non-native nanocrystals can be synthesized inside the resulting hollow interior. Ferritin without a core is called apoferritin.

1.3.1 Applications

Typically, the non-native nanocrystals synthesized inside apoferritin are semiconductors with favorable light emitting and absorbing properties, making them useful in a variety of applications such as biological imaging, nanobiosensors, and photocatalysts. Recent studies at Brigham Young University by Erickson et al. and Watt et al. proposed that nanocrystal-ferritin composites can also be used to absorb photons in solar cells [20,21]; this thesis uses PbS-FTN to expand experimentally on Erickson and Watt's theoretical work.

Hennequin et al. synthesized PbS nanoparticles inside ferritin in 2008. Since then, PbS-FTN has shown to be biocompatible in mice [22] and also an effective inhibitor of cancerous cells [7]. The biocompatibility of PbS-FTN suggests that PbSe and PbTe inside ferritin should also be biocompatible materials that can be used to illuminate tissue. Since PbS, PbSe, and PbTe are narrow gap semiconductors with room-temperature direct band gaps of 0.37 eV, 0.27 eV, and 0.32 eV, respectively, their quantum dot forms have band gaps tunable from ~ 1600 nm to 900 nm, which falls directly into the near-IR window of frequencies most permeable to biological tissue. Although we have not yet synthesized PbTe-FTN, we are currently pursuing this goal.

1.3.2 Synthesis Strategies

To our knowledge, there are three strategies to synthesize non-native nanocrystals inside the apoferritin cavity:

(1) *Ferroxidase center synthesis*: This strategy mimics the natural process of ferrihydrite mineral growth described in Section 1.2. The mineral is allowed to gradually deposit through the ferroxidase center and molecular oxygen is used as the oxidizing agent, similar to ferrihydrite production. Hydrogen peroxide and permanganate have also been shown to work as oxidizing agents [15, 23].

(2) *Cation-Anion synthesis*: This strategy exploits electrostatic gradients on the protein's outer

surface to pull aqueous cations inside the cavity. The strength of these electrostatic effects were discovered computationally by Douglas et al. in 1998 [24]. In practice, exploiting this pathway for crystal growth is simple. First, the cationic portion of the nanocrystal's salt compound is allowed to mix with apoferritin and migrate inside the cavity. Next, the anions are added to solution, which react strongly to form a salt compound with the cations. Since the cations are already housed within the cavity, the crystal growth occurs within ferritin, and is confined by ferritin's inner diameter. Salt formation outside ferritin is unrestricted and results in larger crystals which are typically insoluble and crash out of solution.

(3) *Recombination synthesis*: Lastly, there is a recombination strategy, which consists of breaking up ferritin's subunits and allowing them to reform around pre-synthesized quantum dots. Apoferritin is disassembled into its subunits by exposure to an acidic environment, typically \sim pH 2, and then mixed into a basic or neutral solution of pre-formed quantum dots. The rise in pH causes the separated subunits to recombine, often enclosing a quantum dot in the process. This is usually the least preferred synthesis technique because it can result in incomplete protein recombination [10]. The fact that apoferritin subunits choose to reform around quantum dots is interesting, and suggests that filled ferritin is a preferred state of lower chemical energy than apoferritin.

1.4 Quantum Dots

Quantum dots, synonymous with semiconductor nanoparticles, are nanosized spheres typically \sim 2 - 10 nm in diameter. The chemical synthesis of quantum dots is a balance between encouraging crystallization but restricting the growth to ensure the crystals stay nanosized. Using ferritin to confine the growth is only one method, and quantum dots inside ferritin only represent a small fraction of all quantum dot research. More commonly, a chemical capping agent is used to confine crystallization. For example, consider how thioglycerol ($C_3H_8O_2S$) can be used as a capping agent

to restrict the growth of PbS crystals. Colloidal $\text{Pb}(\text{AcO})_2$ and Na_2S crystallize to form PbS, but the addition of thioglycerol can prevent crystals from growing to an insoluble size by having its sulfur group bond into the PbS lattice, while its organic groups block further lead atoms from joining the lattice. Thus in this manner, thioglycerol is a capping agent for the synthesis of PbS quantum dots.

Quantum dots are optically interesting because their band gaps show size dependence, and thus are tunable by synthesizing different radii quantum dots. The band gap of a solid is the energy difference between the highest filled electron energy state (the valence band) and the lowest empty electron energy state (the conduction band). In a quantum dot, the electron states in the conduction band form a continuous wave function that is subject to a potential barrier at the physical edge of the quantum dot sphere. This creates a "particle in a box" effect and shifts the conduction band higher. Similar to a particle in an infinite well, the energy levels are dependent on the inverse square width of the well, or in the case of the quantum dot, the inverse square of the sphere's radius. This quantum confinement effect is seen in the second term of Brus's equation which describes a quantum dot's band gap energy:

$$E(r) = E_{gap} + \frac{h^2}{8r^2} \left(\frac{1}{m_e^*} + \frac{1}{m_h^*} \right)$$

Therefore, the band gap can be fine-tuned by synthesizing different radii quantum dots. One primary goal of this thesis is to experimentally measure the relationship between core size and band gap energy for PbS-FTN, PbSe-FTN, and PbTe-FTN.

1.5 The Dye Sensitized Solar Cell

The mechanism behind dye sensitized solar cells (DSSCs) is quite simple and fundamentally different from traditional p-n junction solar cells. In the later, p-type and n-type semiconductors come together at a boundary called the p-n junction. Electrons from the n-type material that wander across the junction leave behind a static positive charge on the edge of the n-type material, and

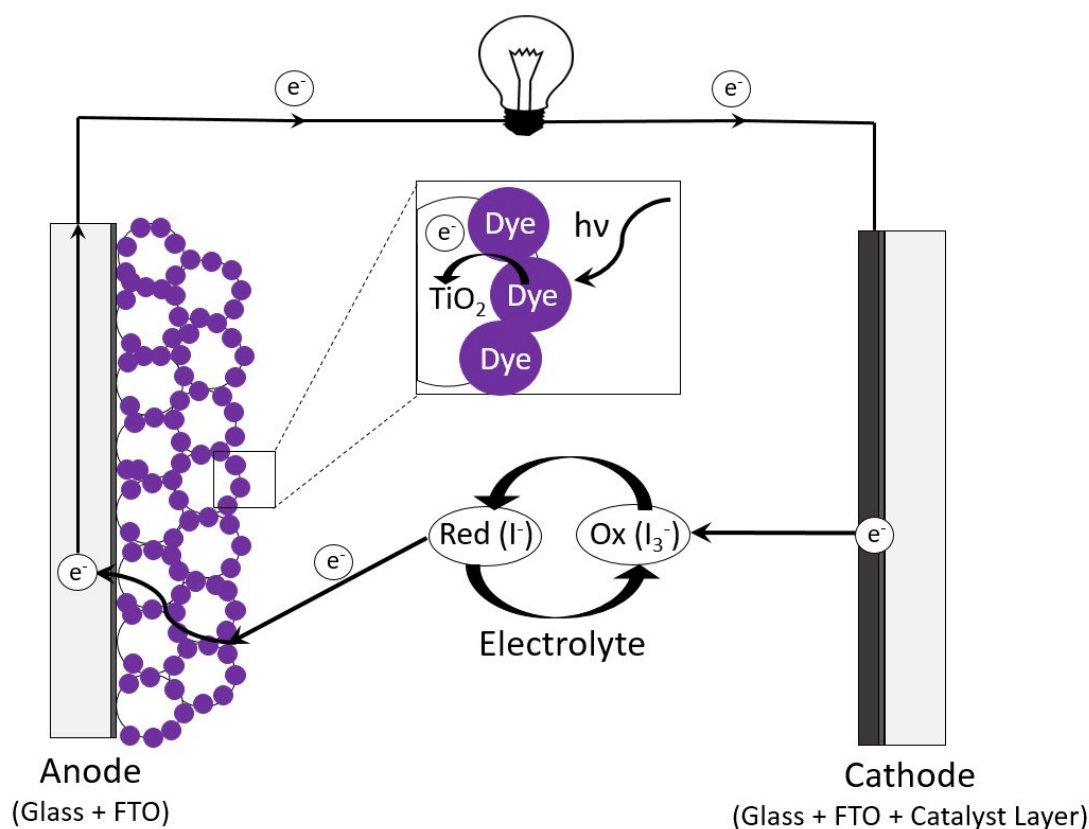


Figure 1.2 The dye sensitized solar cell consists of a dye-stained TiO₂ mesoporous surface wedged between two electrodes. The electrolyte solution completes the circuit by transporting lower energy electrons to holes in the dye molecule, where the electrons can then be re-excited.

eventually recombine with excess holes in the p-type. In a similar manner, holes from the p-type material leave static negative charge on the edge of the p-type material. The accumulation of these static charges on opposite sides of the p-n boundary creates an electric field pointing towards the n-type material. This region is known as the "depletion zone". When incoming sunlight excites an electron, an extra mobile electron and an extra mobile hole are created. The depletion zone's electric field pushes these carriers in opposite directions and generates a current.

The mechanism responsible for photogenerated current in DSSC has two notable differences:

one, there is no p-n boundary, and two, the only mobile charge carriers are electrons. The cell consists of dye molecules (in our case, PbS-FTN) adsorbed to a semiconductor metal oxide (in our case, TiO₂), and mixed with an electrolyte solution. Excited electrons in the dye transfer to the TiO₂ and percolate through the mesoporous surface until reaching an electrode. The electrons perform work and come back to a counter electrode at a lower-energy, where they are accepted by the electrolyte solution and transferred back to the dye molecule in order to fill the holes left behind after photo-excitation. In short, the cell is engineered for excited electrons to prefer recombination by traveling through a circuit, as opposed to radiative recombination. Yet in reality, radiative recombination, along with other loss mechanisms, will occur and prevent the cell from operating at its full potential efficiency².

Since its invention in 1991, the DSSC has been intensely researched due to its potential to be mass-produced using organic materials that are abundant on earth. However, theoretical efficiencies of DSSCs are far from being realized in practice [25]. The theoretical efficiency of a monolayer solar cell is limited to 33.7% by the Shockley-Queisser limit [26]. Solar cells comprised of multiple layers, stacked in order of high-to-low band gap energy (called "multi-junction cells") are more efficient because each layer can collect leftover photons which were not energetic enough to photo-excite the layer above it. Erickson et al. report a three-layer cell, fabricated with ferritin-encapsulated nanocrystals, has a theoretical efficiency limit of 38.0% which rises to 51.3% if a fourth layer with a near-IR band gap (such as PbS-FTN) is added to the bottom [20]. This results demonstrates the importance of finding near-IR photo-absorbers that are functional and stable in a solar cell mechanism. The near-IR band gap energies of PbS and PbSe quantum dots make these materials strong candidates. Furthermore, both materials are known to have highly efficient multiple exciton generation [27], and low exciton recombination rate [28]. The former property is

²To learn about these loss mechanism and much more regarding solar cells, I recommend PVEducation.org ([click here to go there](http://PVEducation.org)).

beneficial because it means one high energy photon has an increased probability of creating multiple charge carriers capable of performing work; the latter property is beneficial because radiative recombination prevents excited electrons from performing work.

Chapter 2

Experimental Methods

2.1 Apoferritin Preparation

To synthesize non-native crystals into ferritin, the natural occurring $\text{Fe}(\text{O})\text{OH}$ mineral must first be removed. We achieved this by allowing a sample of horse spleen ferritin with $\text{Fe}(\text{O})\text{OH}$ cores to mix with thioglycolic acid. The thioglycolic acid removes the $\text{Fe}(\text{O})\text{OH}$ mineral without damaging the protein by forming a soluble iron complex with Fe^{2+} ions and removing them from the ferroxidase center. We put the horse spleen ferritin in a hydrated dialysis cassette with a semipermeable membrane that allows particles of molecular weight less than 7000 g/mol to cross freely. Ferritin at 470,000 g/mol is well above this cutoff value, and therefore remains within the bag during dialysis. For more information on our laboratory procedures, see Section A.1. The modified Lowry method by G.L. Peterson was used to measure protein concentration in the apoferritin after dialysis, typically 25 - 35 mg/mL [29].

2.2 PbS-FTN and PbSe-FTN Synthesis

To my knowledge, the synthesis of PbS-FTN has been reported in three journals articles, all authored by researchers at the University of Nottingham [1, 7, 30]. The synthesis used in these three articles varies the core size by varying Pb:S ratio from 1:0.1 to 1:0.7 and is performed under an inert atmosphere. We base our methods off this procedure, but demonstrate that the reaction can also be run aerobically with a Pb:S ratio of 1:1.

The conditions used to synthesize PbS-FTN nanostructures reported on in this thesis were as follows: 3 mg of apoferritin (92.5 μL of 32.4 mg/mL apoferritin) was injected into 1 mL of 0.1 M sodium acetate buffer at pH 5.5. Although a pH 5.5 sodium acetate buffer was used for all of the samples whose data we show, we note the synthesis is reproducible across a large pH range and without the addition of a sodium acetate buffer.

After preparing the buffer, varying volumes (3.13, 6.25, 12.5, 31.25, 62.5, 125, 250, 437.5, and 625 μL) of 0.1 M lead II acetate $\text{Pb}(\text{C}_2\text{H}_3\text{O}_2)_2$ were inserted to target varying ratios of lead atoms per ferritin proteins (50, 100, 200, 500, 1000, 2000, 4000, 7000, and 10000 leads-per-ferritin). Under moderate mixing, the same quantity of 0.1 M sodium sulfide Na_2S was injected. The samples were then centrifuged at 4000 rpm ($2630 \times g$) for 5 min with Eppendorf 5910 R centrifuge and the supernatant was filtered over a Sephadex G-100 dextran gel filtration column in order to remove non-ferritin quantum dots. All materials were purchased from Sigma Aldrich.

For the synthesis of PbSe-FTN, 0.1 M Na_2Se was used in place of 0.1 M Na_2S . All other steps are the same as the above PbS-FTN synthesis method.

The non-ferritin PbS quantum dots that were used as controls in the photocorrosion experiment (Section 4.2) were synthesized using thioglycerol as a capping agent, as outlined by Bakueva, et al [31].

2.3 MoS₂-FTN Synthesis

The recombination strategy described in Section 1.3.2 was used to create MoS₂ nanocrystals inside apoferritin.

We synthesized aqueous MoS₂ quantum dots in the absence of ferritin. In the literature there are two methods for MoS₂ quantum dot synthesis, namely, a top-down approach that shatters bulk MoS₂ with ultra-sonification, and a bottom-up approach where the quantum dots crystallize from chemical vapour deposition [32]. We used the bottom-up hydrothermal chemical vapour deposition method by Yong Wang et al. [33].

First, 0.25 g of Na₂MoO₄·2H₂O were dissolved into 25 mL of distilled water (dH₂O), sonicated for 5 minutes, and then adjusted to pH 6.5 with 0.1 M HCl. Next, 50 mL of dH₂O and 0.5 g of *L*-cysteine were mixed in, followed by sonication for 10 min. A Heat Systems ultrasonic processor was used at level 10 for the sonication. Next, the solution was transferred to a Pyrex beaker with a tin-foil cap and placed in an autoclave for ~24 hours at 150°C¹. The solution was allowed to cool naturally, and the resulting supernatant containing MoS₂ was collected after centrifuging for 5 min at 4000 rpm (2630 × *g*). Next, 2 mL of the resulting solution was then filtered over a Sephadex G-100 filtration column and collected in 1 mL fractions. The two fractions with the highest absorption were combined (fractions 5 and 6). 25 mmol pH 8.5 Tris was used as the gel-filtration buffer.

Apoferritin was disassembled by dialysis against an acidic buffer. 2.5 mL of apoferritin prepared according to Section A.1 were injected into a new hydrated dialysis cassette and mixed for 8 hours against 1 L of 0.1 M NaCl solution that was adjusted to pH 2 with HCl.

Finally, the disassembled apoferritin and MoS₂ quantum dots were combined to form MoS₂-FTN: 0.15 mL of the pH 2 disassembled apoferritin was inserted into 0.25 mL of the filtered MoS₂ quantum dots under moderate mixing.

¹Yong Wang's method calls for a 36 hours at 200°C reaction inside an autoclave; however, BYU autoclave's pressure was such that any longer than 20 hours at 140°C resulted in complete evaporation and loss of sample.

2.4 Gel-Filtration Chromatography

We filtered nanocrystal-ferritin samples through a 15 cm \times 1 cm Sephadex gel gravity column in order to split samples into fractions ordered by solute size. The Sephadex gel is a chemically inert matrix of small, porous polymer beads of varying size. Smaller molecules are trapped inside pores within the polymer bead matrix, whereas molecules above the gel's cutoff size are allowed to pass through at a uniform speed. Since proteins are biologically produced, the size of each ferritin is extremely uniform, making gel-filtration chromatography an effective method to isolate ferritin-sized molecules from excess salts also in the solution. In our case, the Sephadex G-100 (medium) with bead sizes 40-120 μm works well to isolate ferritin.

After a given synthesis, nanocrystal-ferritin samples were centrifuged at $2630 \times g$ for 5 minutes, the supernatant was extracted, placed in the gravity column, and collected in 1.25 mL fractions. 25 mM Tris at pH 8.5 was used as a buffer. For more details on our gel-filtration experimental procedures, see Appendix Section A.2.

2.5 Protein Quantification

Measuring the protein and metal atom concentrations (section 2.6) of our samples provide us a high-throughput method to estimate the average core size in each sample. To measure protein concentration, we used both the Bradford and modified Lowry protein assays [34, 35]. Both methods rely on appreciably complicated chemical reactions between the protein and the active reagent that induce a color change dependent on the overall protein concentration. The protein concentration can then be calculated by measuring each sample's absorbance at the wavelength of light most affected by the color shift (750 nm for Lowry, 580 nm for Bradford), and then comparing the absorbance to a standard of known protein concentration.

For our purposes, the two methods have distinct pros and cons. The Lowry method is more ac-

curate for measuring ferritin concentration because the spherical shell is denatured and each amino acid is exposed to the reagent, allowing for consistent and accurate detection of the protein concentration. The Lowry method's downside, however, is that the active reagent can be significantly affected by various molecules present in the nanocrystal-ferritin samples. The Bradford method is less susceptible to interference by non-protein molecules; however, unlike the Lowry method, the Bradford method does not accurately measure ferritin concentration. The ferritin is not denatured, and therefore only the outside surface of the protein is allowed to react with the Bradford agent, resulting in a color change that isn't representative of the total protein concentration.

The inaccuracy of the Bradford method is of serious issue when determining overall metal-to-ferritin ratio, such as the values reported in Figure 3.1, because this ratio depends on the overall number of ferritin. In these cases, the inaccuracy of the Bradford method can be accounted for by using a calibrated apoferritin control. Apoferritin's concentration can be accurately determined by the Lowry method, Beer-Lambert's law, or both.

To calculate the apoferritin concentration with Beer-Lambert's law, we use:

$$A = \epsilon cl$$

where A is the absorbance, ϵ is the molar extinction coefficient, c is the concentration, and l is the light's path length. It is known that $\epsilon = 471,000 \text{ cm}^{-1} \text{ M}^{-1}$ for apoferritin illuminated by 280 nm light [36]. Thus, the concentration can be directly calculated after measuring the absorbance at 280 nm and the light's path length through the sample.

After apoferritin's concentration is accurately determined with Beer-Lambert's law, the Lowry method, or both, the same apoferritin sample can be used to calibrate ferritin concentrations in nanocrystal-ferritin samples measured with the Bradford method.

2.6 Metal Quantification

To measure the overall concentration of metal atoms of each sample, we use inductively coupled plasma mass spectrometry (ICP-MS).

The nanocrystal-ferritin constructs are dissolved in nitric acid (HNO_3), centrifuged, and filtered in order to purify the sample for the ICP-MS machine. Within the ICP-MS, metals are ionized within a plasma, and sorted through an electric quadrupole filter according to their charge-to-mass ratio. At the end of the quadrupole filter, a detector receives an ion signal proportional to the sample's concentration of metal atoms. The ion signal as a function of the charge-to-mass ratio is compared to calibrated metal samples, and the overall concentration of metal atoms is calculated.

For more details regarding ICP-MS sample preparation, see Appendix Section A.3.

2.7 TEM analysis

High resolution TEM (HRTEM) images were taken in both STEM and bright-field modes using a Tecnai-F20 TEM. TEM sample preparation consisted of depositing the samples onto a carbon type-b 300 mesh copper grid and applying a uranyl acetate stain in order to illuminate the protein shell. For more details on sample preparation, see Appendix Section A.4.

2.8 Photoluminescence

Since PbS is a direct-gap semiconductor, the band gap energy can be measured by excited photoluminescence. Incoming photons excite valence electrons in the material to an energy higher than the band gap. The electrons relax to the bottom of the conduction band and then undergo "radiative recombination", meaning the electron falls from the conduction band to the valence band and emits a photon characteristic of the band gap.

To prepare samples for PL measurements, aqueous samples were deposited on glass slides and illuminated with a 398 nm continuous wave diode laser at 100 mW. The laser was modulated at 5 kHz in order to use a lockin amplifier in conjunction with a photodiode detector. The resulting PL spectrum was adjusted for the Teledyne Judson J16D germanium photodiode detector responsivity.

Each nanocrystal-ferritin sample has a Gaussian distribution of core sizes, the width of which is roughly represented by the width of the PL spectrum (since the band gap is dependent on the core radius as described in Section 1.4). The wavelength of light at the PL's peak was recorded as the sample's average band gap energy.

2.9 Solar cell fabrication

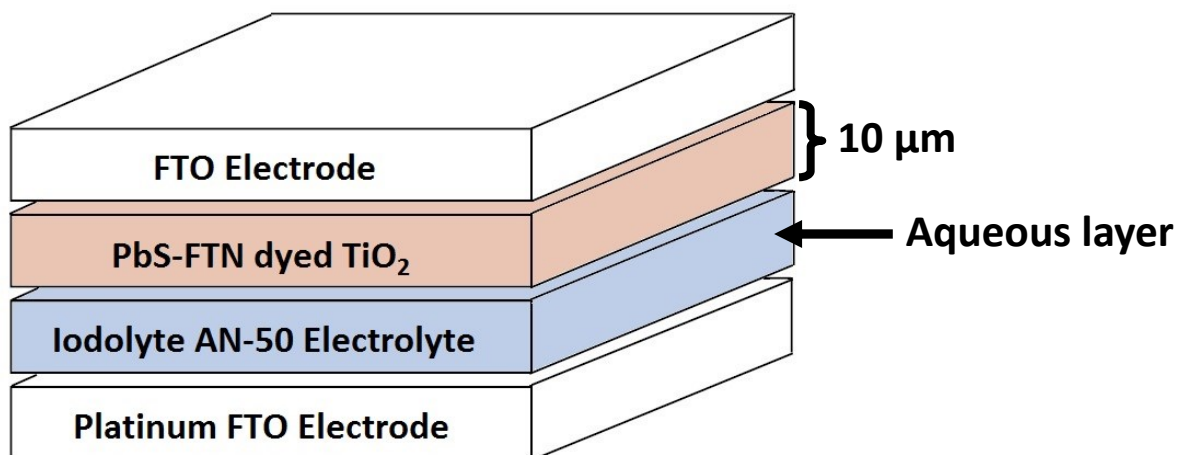


Figure 2.1 Schematic of the dye-sensitized solar cell. Binding between PbS-FTN dye and TiO₂ layer is a critical factor in determining photovoltaic performance.

Fabrication of DSSCs with non-ferritin PbS quantum dots as the dye is well-established [37, 38]. To our knowledge, binding between the mesoporous TiO₂ and PbS quantum dots has been accomplished using two methods: 1) immersion of annealed TiO₂ electrodes into pre-synthesized

aqueous PbS quantum dots and more commonly 2) successive ion layer adsorption and reaction process (SILAR) [39,40]. We experimented mimicking these techniques with PbS-FTN in place of PbS with the goal of achieving strong binding between the PbS-FTN dye and mesoporous TiO₂ layer. In addition, we used two other methods, for a total of four methods:

Method 1, direct immersion: The TiO₂ electrode was immersed in PbS-FTN solution for 72 hours. *Method 2, SILAR:* Successive ionic layer adsorption and reaction [39] was performed using ferritin-encapsulated lead acetate as the cation solution and Na₂S as the anion solution. The cation solution was prepared by mixing 12 mg of apoferritin (0.37 mL of 32.4 mg/mL apoferritin), 0.5 mL 0.1 M Pb(C₂H₃O₂)₂, and 5 mL dH₂O. The anion solution was 0.01 M Na₂S. One cycle consisted of immersing the electrode face-up in the cation solution for 2 minutes, rinsing thoroughly with dH₂O, immersing in anion solution for 2 min, and then rinsing again. *Method 3, electrophoresis:* Titanium and platinum electrodes were clamped parallel and 1 cm apart separated by a dielectric spacer and suspended in 0.1 mg/mL PbS-FTN. An SRS DS340 waveform generator was used in DC mode to generate a stable 0.8 mA current (0.4 mA/cm²) between electrodes at 4.5 V for 25 minutes [41]. *Method 4, drop cast:* One drop of highly concentrated PbS-FTN (12 mg/mL protein concentration) was deposited on the TiO₂ surface and allowed to dry.

Opaque titanium FTO electrodes, transparent platinum FTO counter electrodes, and Iodolyte AN-50 electrolyte solution were purchased from Solaronix. Titanium electrodes were annealed at 450°C for 30 minutes to remove impurities. TiO₂ and Pt electrodes were assembled following methods similar to those outlined by Solaronix [42].

2.10 IV measurements

Fabricated DSSCs were placed under full sun equivalent illumination using a 150 W Xe arc lamp at standard AM 1.5 condition (100 W/cm²) [43]. IV measurements were recorded with a Fluke

8840A/AF multimeter using a variable resistance load of 5 - 5000 Ω .

Chapter 3

Synthesis Results and Discussion

3.1 PbS-FTN

PbS core formation inside ferritin was achieved for all tested ratios of lead atoms per ferritin, abbreviated "leads-per-ferritin" for simplicity. Core formation of soluble PbS-FTN was indicated by a permanent red-brown color which persisted after centrifugation and further confirmed by HRTEM images of aqueous solutions. Figure 3.1 shows the average number of lead atoms per ferritin for samples 1 - 9, in which targeted ratios spanned from 50 - 10,000 lead atoms per ferritin. As expected, the core sizes increased according to the targeted lead count in samples 1 - 6; however, samples 7 - 9 show an inverse trend due to overloading. The synthesis reported by Hennequin, et al. is performed under an inert atmosphere and varies the Pb:S ratio from 1:0.1 to 1:0.7 to achieve core diameters $2 - 8 \pm 2$ nm (measured by TEM, details below). Following these methods, we achieved average core diameters ranging from $2.51 - 5.92 \pm 1$ nm. In order to test the effects of performing the synthesis in an inert atmosphere and with a Pb:S ratio >1 , we performed three synthesis assays: one anaerobically at 1:1 Pb:S ratio, and one aerobically at 1:1 Pb:S ratio, and one anaerobically with 1:1 Pb:S ratio. Our results indicate that an inert atmosphere and Pb:S ratio

greater than 1 both have little or no effect on resulting quantum dot size or stability.







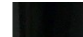







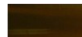
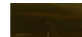
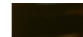
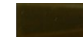





Sample Number	1	2	3	4	5	6	7	8	9	
Targeted Lead/FTN	50	100	200	500	1000	2000	4000	7000	10000	
Aerobic Synthesis										
Lead/FTN	34 ± 4	106 ± 17	151 ± 25	299 ± 56	811 ± 210	2552 ± 612	1982 ± 445	1266 ± 264	1133 ± 197	
Band-Gap Energy	1.33	1.25	1.23	1.14	1.03	1	1.11	1.22*	1.30*	
Color										
Anaerobic Synthesis										
Lead/FTN	37 ± 7	63 ± 11	136 ± 20	367 ± 63	865 ± 180	2611 ± 483	1187 ± 399	724 ± 121	690 ± 169	
Band-Gap Energy	1.33	1.21	1.14	1.12	1.06	0.97	1.08	1.24*	1.05*	
Color										
3 × Lead Anaerobic Synthesis										
Lead/FTN	36 ± 7	74 ± 8	181 ± 10	
Color				

Figure 3.1 Summary of both anaerobically and aerobically synthesized PbS-FTN samples. Sample color was photographed after gel-filtration, which diluted samples to equal volumes. The error in leads-per-ferritin ratio includes both measurement and statistical error. The band gap energy and leads-per-ferritin was not measured for all samples in the 3× lead assay due to metal overloading in samples 4 - 9. No PbS core formation was observed in these samples.

Targeted leads-per-ferritin ratios in Figure 3.1 were chosen to yield theoretical core diameters ranging from 1.71 - 9.99 nm. Assuming an ideal case where injected lead atoms are evenly distributed across all the injected ferritin proteins, an upper bound for the average core radius can be estimated by setting crystal volume equal to the spherical volume:

$$\frac{4\pi}{3}R^3 = \frac{1}{4} \frac{N_{lead}}{N_{ferritin}} a^3$$

where R is the core radius and a is PbS's lattice constant. The factor of $\frac{1}{4}$ comes from PbS's halite

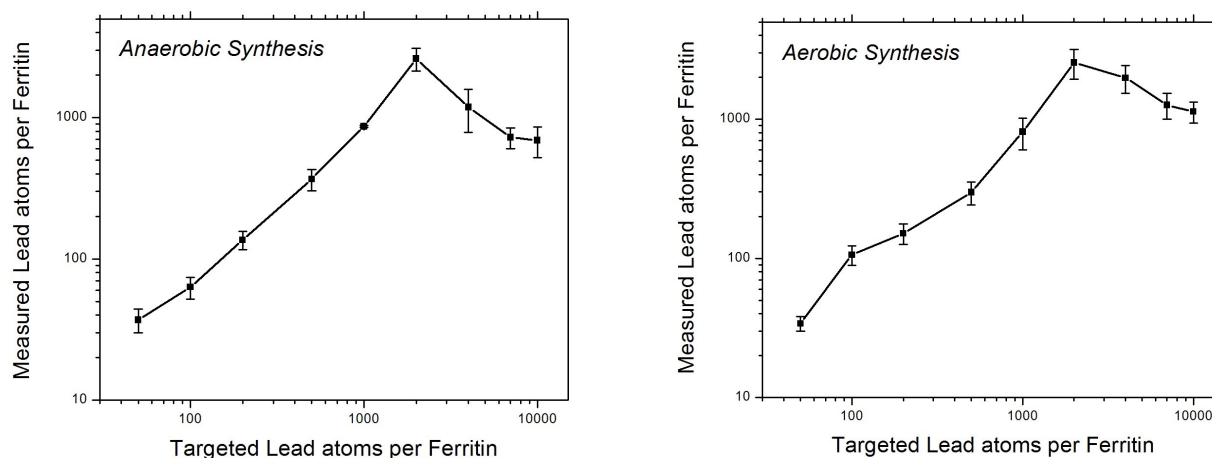


Figure 3.2 Comparison of PbS-FTN synthesis run under inert vs oxygen atmosphere. Only minor differences within the expected error margin were observed.

FCC crystal structure which has 4 lead atoms per unit cell. Although not all core formation inside ferritin grows spherically, our TEM images reveal that PbS nanocrystals do. Comparing the synthesized core sizes to this idealized upper bound reveals information about the chemical mechanism of the PbS-FTN synthesis. For example, sample 1's average core diameter was measured with HRTEM to be 2.25 ± 0.48 nm which is higher than the upper bound predicted by equation 1. Thus, after the reaction, many of the ferritins were left empty causing a higher metal-to-ferritin ratio in PbS-filled ferritins, and indicating a certain level of affinity between the lead atoms when entering ferritin's transport channels. Since empty ferritin and PbS-FTN are the same size, the empty ferritins likely persisted in solution after passing through the size-separating column, and thus were included in the Bradford protein measurement. Any apoferritin included in protein quantification would decrease the measured leads-per-ferritin ratio. This reason, along with inevitable PbS crystallization outside of ferritin, are likely explanations as to why measured leads-per-ferritin ratios are lower than targeted in samples 1 - 5 (Figure 3.1).

Metal atom concentrations were chosen primarily for a 1:1 Pb:S ratio, so it is not surprising

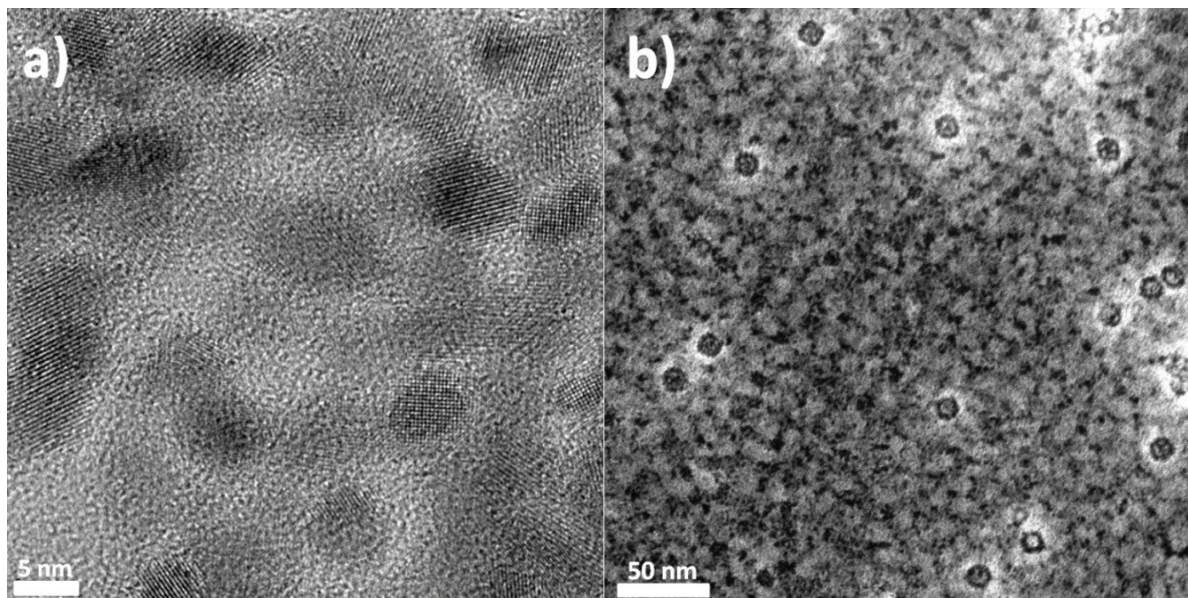


Figure 3.3 (a) Unstained sample 6 (anaerobically synthesized). Bright-field TEM image acquired on Tenaci-F20 TEM. Uniform lattice fringes with PbS's 0.59 nm lattice constant and spanning 4 - 7 nm diameters clearly reveal quantum dot sizes. (b) Uranyl-acetate stained sample 7 (aerobically synthesized), image acquired in STEM mode at 1.15 Mx spot size 9. The dark circular protein shell surrounding the illuminated nanocrystal interior shows successful incorporation of quantum dots into the hollow apoferritin.

that the $3\times$ lead assay failed for samples 4 - 9 due to overloading. This was expected since other nanocrystal-ferritin studies report poor quality quantum dots at extremely high metal atom concentrations [23,44]. Still, samples 1 - 3 in the $3\times$ lead assay are indicative of the 3:1 Pb:S ratio's effect on the synthesis, since the overall leads-per-ferritin ratio in these samples is well under the known limit. For this synthesis, no significant difference in the sample's color nor the sample's leads-per-ferritin ratio was observed, see Figure 3.1, $3\times$ lead anaerobic.

Due to the Gaussian distribution of core sizes in each sample, some diameter >7 nm quantum dots were present in samples 5 - 8; however, it proved difficult to synthesize a sample with an average quantum dot diameter >7 nm. The largest average core size measured was aerobically synthesized sample 6 at 6.10 nm with standard deviation of 0.89 nm.

Core diameters were measured using bright-field TEM images similar to Figure 3.3 (a). Images

taken in STEM mode (3.3 (b)) were used to verify quantum dots position inside the ferritin shell. STEM mode images displayed significantly larger core diameters (~ 2 nm larger, or $\sim 35\%$) than bright-field images even though a calibration check showed a minor $\sim 3\%$ disagreement between scale bars produced under STEM and bright-field modes. The cores in STEM images likely appear larger due to the Gaussian distribution within the microscope's electron beam. As the edge of the finite-width electron beam rasters over the edge of a spherical core, it will prematurely scatter electrons and record high intensity [45]. The core diameters measured in bright-field parallel beam mode are more likely representative of the true size. The lattice fringes caused by electron phase contrasting clearly reveal a circular form.

The shape of small-diameter PbS quantum dots observed in TEM bright field images reveals information about the chemical process of PbS core formation. The most natural mechanism for core formation in ferritin involves gradual nanocrystal growth on H-chain nucleation sites. Lopez-Castro, et al. have shown that for H-chain dominated ferritins (such as the equine spleen ferritin used in this study) core formation via this mechanism results in shell-shaped coating of ferritin's inner radius [18]; however, this is not what we observe. The presence of enclosed quantum dots with a spherical diameter smaller than ferritin's inner diameter indicates that PbS core formation inside ferritin likely occurs by an electrostatic gradient as described by Douglas, et al [24].

3.2 **PbSe-FTN**

The PbSe-FTN synthesis behaved similar to PbS-FTN, except that larger cores proved more difficult to synthesize. The maximum average number of lead atoms per ferritin protein was 2611 for PbS and only 404 for PbSe. We lack sufficient data to describe the relationship between core size and band gap energy for PbSe-FTN; however, this is a goal we are currently actively pursuing. Since PbSe is also a direct gap semiconductor, we expect the band energy to be measurable from

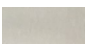
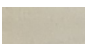



Sample Number	1	2	3	4	5
Targeted Lead/FTN	50	100	200	500	1000
Lead/FTN	54 ± 9	106 ± 8	132 ± 36	183 ± 32	404 ± 60
Color					

Figure 3.4 (Left) The elution profile, as measured by absorbance at 480 nm, for PbSe samples 1 - 5. (Right) The elution profile, as measured by metal and protein concentrations, for PbSe sample 4.

photoluminescence experiments as described in Section 2.8.

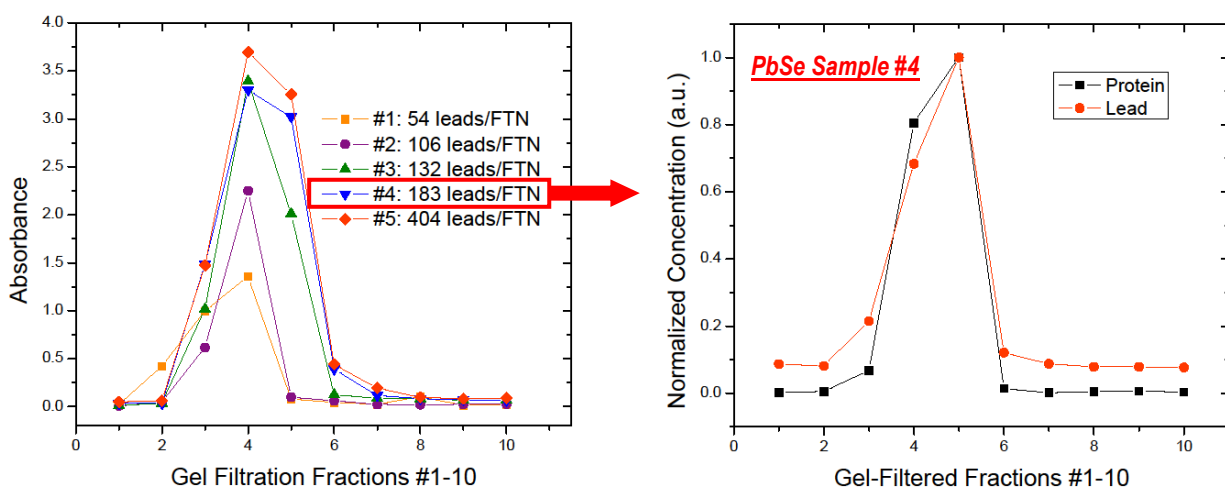


Figure 3.5 (Left) The elution profile, as measured by absorption, for PbSe samples 1 - 5. (Right) The elution profile, as measured by metal and protein concentrations, for PbSe sample 4.

Figure 3.5 above, along with TEM images in Figure 3.6, provide strong evidence that PbSe nanocrystals successfully formed inside ferritin. Figure 3.5 (right) shows the lead and protein concentrations peak at the same 1 mL fraction, demonstrating that the lead atoms are inside ferritin. Selenium atoms must also be inside ferritin because the addition of Na_2Se induces a distinct color change, demonstrating PbSe crystallization. This color persists after gel filtration, as seen in Fig-

ure 3.5 (left): the peak in absorbance occurs corresponds to the peaks seen in lead and protein concentrations (fractions 5 and 6).

3.3 MoS_2 -FTN

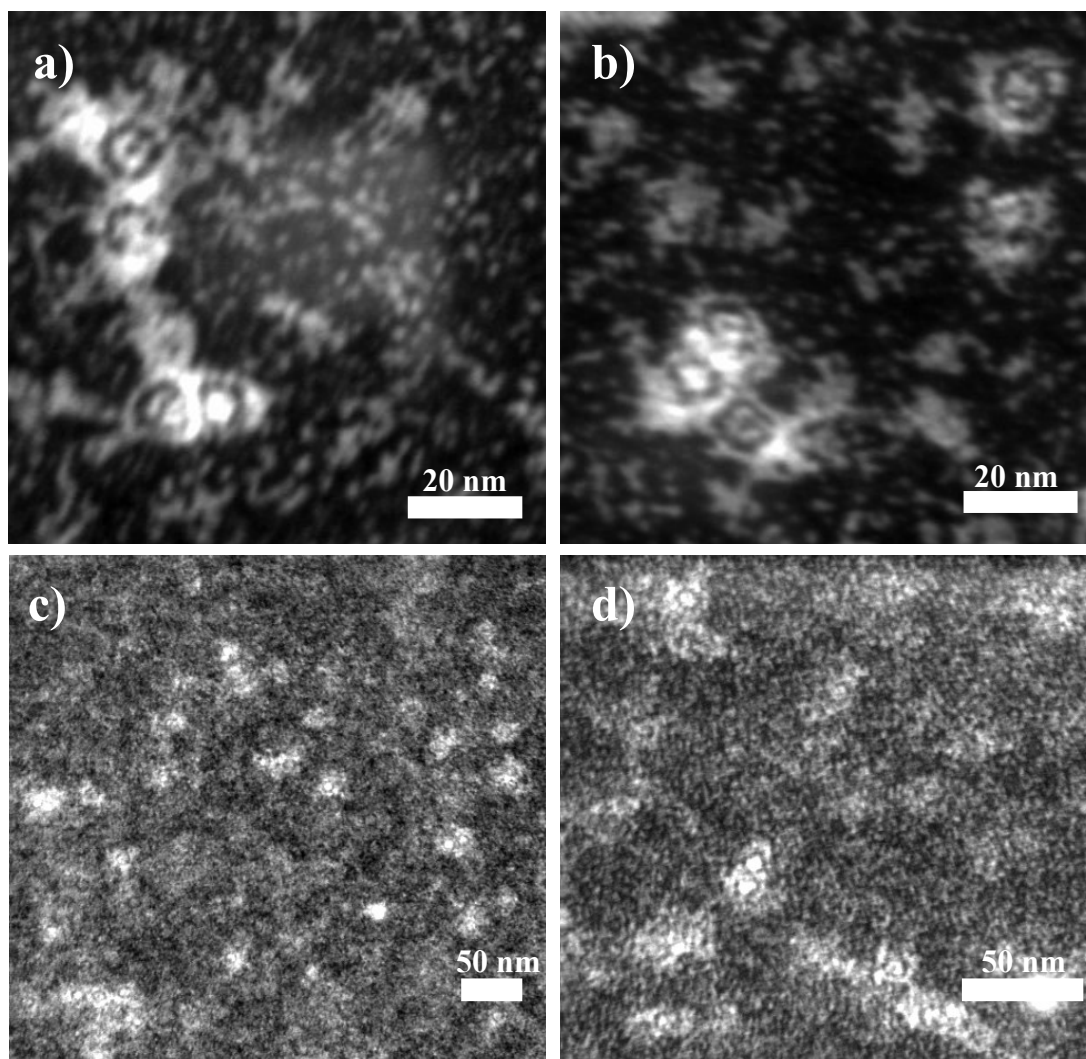


Figure 3.6 (a) and (b) Images of PbSe sample 4 stained with uranyl acetate, acquired on Tenaci-F20 TEM in STEM mode. (c) and (d) Images of Mo_2S prepared and imaged in the same manner. Although none of these images are publication quality, they show successful incorporation of the nanocrystals into the ferritin shell.

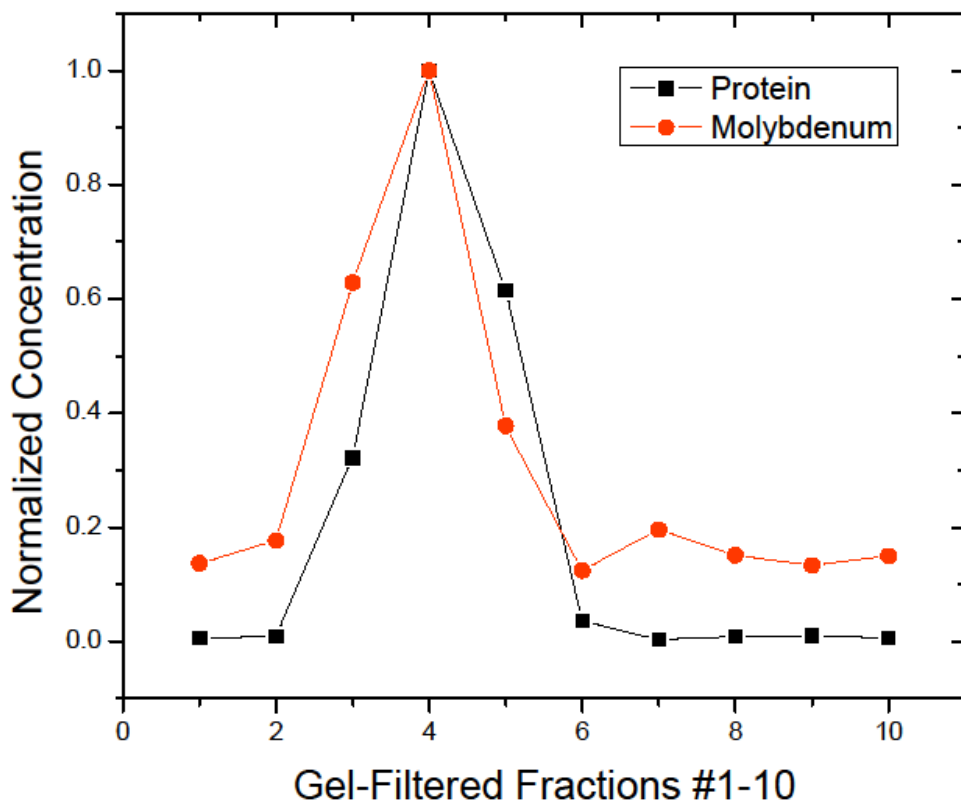


Figure 3.7 Elution profile of MoS₂-FTN showing the metal and protein simultaneously fall through the size-filtration gel matrix at the same rate. Since molybdenum atoms are much smaller than the protein, this demonstrates the majority of molybdenum atoms in are sample are inside ferritin's shell.

Similar to PbSe-FTN, data are still being collected for MoS₂-FTN. We hope to optimize the synthesis and map the relationship between core size and band gap energy. Also similar to PbSe-FTN, our confidence that we synthesized MoS₂-FTN quantum dots comes from two pieces of evidence: TEM images (Figure 3.6), and an elution profile of our sample that shows simultaneous peaks for metal and protein concentrations (Figure 3.7).

Chapter 4

Optical Characterization: Results and Discussion

4.1 Photoluminescence

PL sample preparation involved depositing liquid PbS-FTN samples on a glass slide and allowing the water to evaporate, as described in Section 2.8. Inconsistent PL data from these slides led to the discovery that the droplet evaporation did not leave a homogeneous layer of quantum dots; rather, most of the quantum dots dried in a tightly-packed, thin ring along the edge of the droplet, and it was noticed this ring of quantum dots provided a higher quality PL signal at an energy slightly lower than quantum dots dried at the center. The PL seen in Figure 4.1 was acquired by illuminating quantum dots at the center of the droplet.

As seen in Figure 4.1, the band gaps ranged from 1.33 - 0.98 eV for PbS-FTN samples 1 - 6. Samples 7 - 9 were overloaded with lead and sulfur (Figure 3.2); these poor quality quantum dots showed less coherent and wider PL peaks, and therefore were omitted from Figure 4.1 and not studied further.

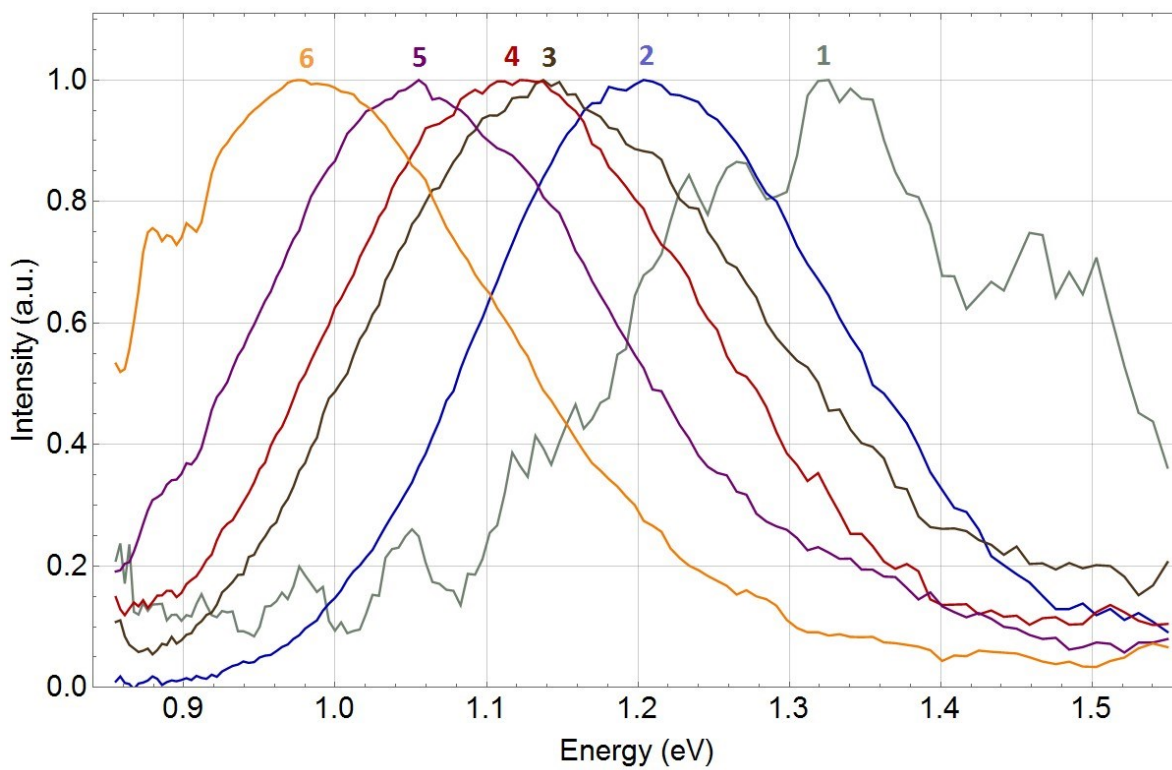


Figure 4.1 Photoluminescence of aerobically synthesized samples 1 - 6 at room temperature. The band gap energy is inversely proportional to quantum dot size, as described by the Brus equation in Section 1.4. Samples 7 - 9 for all assays generally had inconsistent and low-intensity PL signals.

4.2 Photocorrosion: PbS vs PbS-FTN

The stability of PbS-FTN quantum dots was compared to PbS quantum dots after 30 min of exposure to a 398 nm continuous wave 100 mW laser. Figure 4.2 shows burn marks are visible on PbS quantum dots synthesized with thioglycerol, but not visible on the PbS-FTN; this supports the hypothesis that ferritin-encapsulation protects PbS quantum dots from photocorrosion.

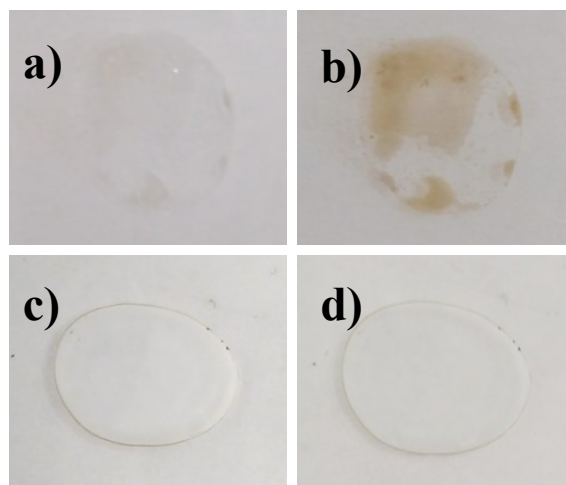


Figure 4.2 Comparison of photocorrosion in non-ferritin (a,b) vs ferritin (c,d) PbS quantum dots. Burn marks the size of the beam's width are noticeable in non-ferritin samples after 30 min of exposure to a 398 nm continuous wave 100 mW laser. Little to no corrosion is visible on PbS-FTN samples.

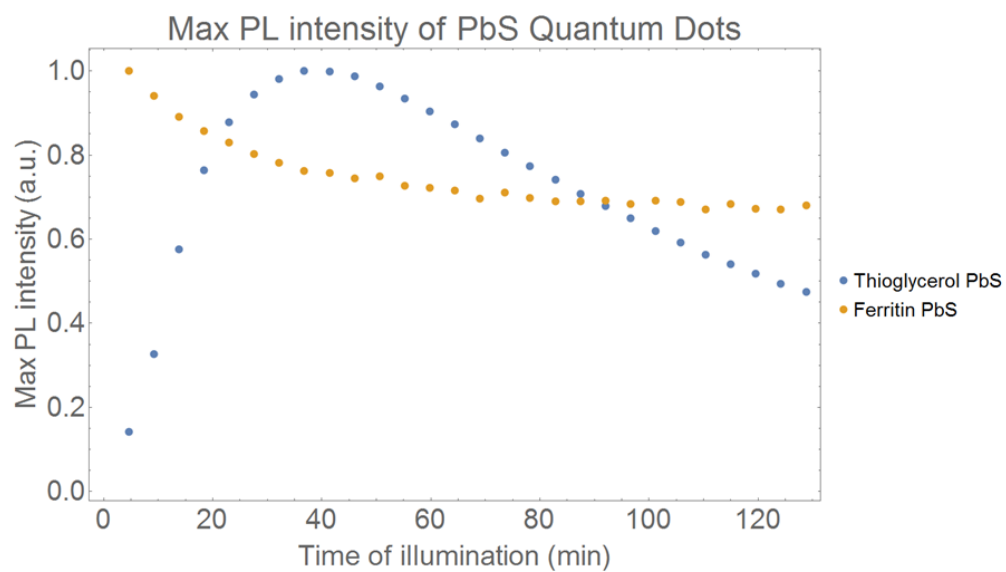


Figure 4.3 A comparison of time-evolved photoluminescence for PbS quantum dots and PbS-FTN. Samples were illuminated with a 398 nm diode laser at $\sim 10 \text{ W/cm}^2$.

The time evolution of the PL signal for both materials was also studied by measuring PL signals at 5 minute intervals for 140 minutes. Figure 4.3 shows how the peak intensity of each spectra evolved over time. The non-ferritin PbS sample underwent a more drastic evolution and ended at a lower intensity than PbS-FTN. Furthermore, the continual downward slope of the non-ferritin PbS at 140 minutes suggests that the intensity will drop lower under longer exposure, in contrast to the PbS-FTN which appeared to stabilize at $0.75\times$ the original intensity after 70 minutes.

The durability of PbS-FTN in photochemical reactions is likely due to ferritin's ferroxidase center. The ferroxidase center, described in Section 1.2, is a catalytic site at the center of the H subunits that prevents loose Fe^{2+} ions from exiting the protective confines of the ferritin shell and re-synthesizes them into the $\text{Fe}(\text{O})\text{OH}$ mineral. It's believed that the ferroxidase center can perform the same activity for non-native cores, such as PbS [21]. This "self-healing" property of ferritin is of obvious benefit for photovoltaic applications.

4.3 IV Performance

As detailed in the Section 2.9, we tested four PbS-FTN to TiO_2 adsorption techniques: direct immersion, SILAR, electrophoresis, and drop-cast. The results for each method's highest performing cells are displayed in Figure 4.4. The open current voltage (V_{OC}) is the maximum voltage measured when the current through the solar cell is zero; the short-circuit current density (J_{SC}) is the highest current density measured (occurs when the applied series resistance is at a minimum). Multiplying V_{OC} and J_{SC} yields the maximum power of an ideal solar cell, and can be visualized as the minimum area on an IV plot required to enclose all of the cell's data points (with the requirement the area must be square-shaped). Dividing the actual maximum power by this number results in the fill factor (FF), a parameter used to indicate the cell's quality.

In general, each method's performance was quite variable and difficult to reproduce consis-

Device	V_{oc} (V)	J_{sc} (mA cm^{-2})	FF (%)	η (%)
Control (Anthocyanin)	0.41	0.95	73.2	0.44
PbS-FTN Immersion	0.37	0.90	55.8	0.26
PbS-FTN SILAR	0.23	0.72	47.1	0.11
PbS-FTN Drop Cast	0.58	0.52	64.1	0.28

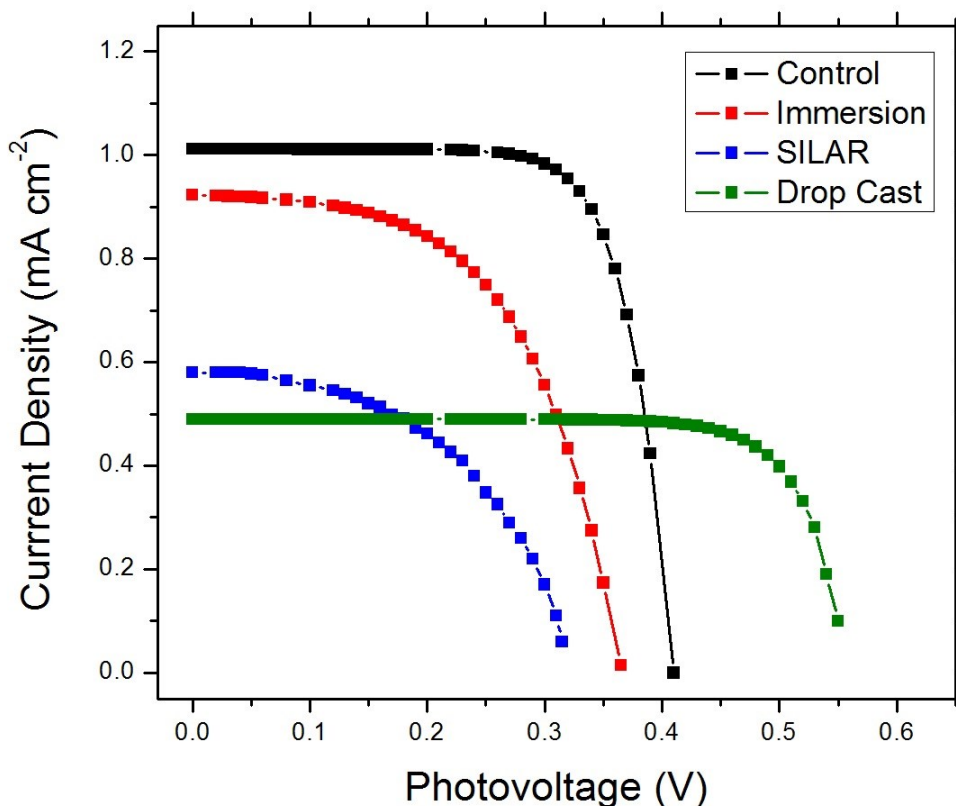


Figure 4.4 IV-plot showing photovoltaic performance of PbS-FTN in DSSCs. The control is an anthocyanin-dyed DSSC fabricated using the same materials.

tently. Drop-cast and direct immersion yielded the highest quality solar cells, with efficiencies 0.28% and 0.26%, respectively (see Figure 4.4). SILAR-adsorbed substrates had worse performance. Furthermore, with the SILAR method, we were unable to conclusively determine whether

adsorbed PbS quantum dots were or were not inside the ferritin shell, since the lead-FTN solution could have free lead ions present. Electrophoretic deposition was performed in ferritin concentrations varying from 0.1 to 0.9 mg/mL. In the presence of an applied voltage, a distinct color change on the TiO₂ surface was apparent; however, upon removal from the circuit, the TiO₂ returned to the original white color, indicating that with the electrophoretic deposition no permanent ferritin-TiO₂ bonds were formed.

When considering the open circuit voltage and short circuit current, the PbS-FTN and anthocyanin solar cells were close in performance. PbS-FTN's lack of efficiency is due to the non-ideal IV shape caused by a high series resistance, which could be caused by many sources: weak ferritin-TiO₂ binding, non-ideal electron transfer dynamics between the core and ferritin and/or between ferritin and TiO₂ layer, an ineffective reduction reaction between the electrolyte and PbS quantum dots, etc. Preliminary studies of non-ferritin PbS DSSCs by Plass et al. reported 0.49 % efficiency [37], and later in 2012, this efficiency increased to 3.5% [46], so improvement is expected as cell fabrication techniques are optimized. Furthermore, our anthocyanin control's efficiency was much lower than measured by other groups, suggesting improvements in cell fabrication would also increase the performance of the PbS-FTN [47–49]. Sources of error in our cell fabrication can potentially be ascribed to electrolyte quality, impurities in solution and TiO₂ surface, applied pressure between electrodes, TiO₂ substrate thickness, etc. These variables were controlled for, but not optimized.

Chapter 5

Conclusions

5.1 Summary

PbS, PbSe, and MoS₂ quantum dots were successfully synthesized inside ferritin. The PbS-FTN assay showed core diameters ranging from 2.25 - 6.10 nm and corresponding band gap energies 1.33 - 0.98 eV. Our results demonstrate that elimination of the inert atmosphere and 3:1 Pb:S ratio from the synthesis has no noticeable effect on the quantum dot size or optical properties of PbS-FTN.

By comparing the time-evolved PL between PbS-FTN and thioglycerol-capped PbS quantum dots, we conclude ferritin-encapsulation protects the PbS quantum dots from photocorrosion. DSSCs were fabricated using the PbS-FTN constructs as the dye and IV measurements showed our highest performing cell has 0.28% efficiency and 64.1% fill factor.

TEM analysis and metal/protein quantification of PbSe and MoS₂ samples demonstrates that these nanocrystals were successfully synthesized inside of ferritin. More work on is currently being done in order to, one, optimize the synthesis, and two, measure the relationship between core size and band gap energy for PbSe-FTN and MoS₂-FTN.

5.2 Future work

5.2.1 Micro-PL and Micro-photocurrent Experiments

As mentioned in Section 1.5, non-ferritin PbS quantum dots tend to cluster when adsorbed onto the TiO₂ substrate, and this creates a non-ideal spatial dependence in the material's photovoltaic response. It's plausible that the ferritin shell can act as template in order to space out the quantum dots and prevent clustering.

The primary goal of this future experimental setup is to create 2D surface plots of PbS-FTN DSSCs, or any other type of cell, where the intensity or color of each point represents the photogenerated current produced by illuminating that location on the cell. The setup can easily be extended to also record the excited PL at each location. Below is an excerpt from an ORCA proposal in which this experiment is described, using materials available in Dr. John Colton's laboratory:

Solar cells will be mounted on two translational stages with the ability to move with 10 μm step size on two axes. A 1000 \times objective lens will be used to focus a 398 nm Thorlabs continuous wave diode laser down to a beam width of $\sim 5 \mu\text{m}$ on the surface of the solar cell. The excited photoluminescence and photo-generated current will be measured simultaneously using lock-in amplification and recorded to a LabVIEW VI. The laser's intensity is a critical variable that must be considered—too low will result in undetectable current, too high will burn the cell. Calculations based off PbS-FTN DSSC IV-measurements reveal that in order to obtain a detectable photo-generated current (1 - 10 nA), we will need a minimum of laser intensity of $\sim 2 \mu\text{W}$, which is obtainable by attenuating the 100 mW beam before the objective lens. Spatial photocurrent and PL plots will be generated for all three types of solar cells, and the spatial homogeneity will be compared to non-ferritin PbS DSSC reported by Turyansk, et al [9].

Through this manner, we can probe the spatial homogeneity in both photocurrent and PL for solar cells of interest. This experiment, along with HRTEM analysis of ferritin-encapsulated

nanocrystals adsorbed on TiO₂, will be important steps towards understanding binding between ferritin and TiO₂¹.

5.2.2 Crystalline Ferritin Device

It may be possible for ferritin-based quantum dots to function as solar energy converters in devices other than DSSCs. Recent work by P.A. Sontz and Jake Bailey at UC San Diego showed genetically modified ferritin can be linked into a BCC crystalline framework that easily self-assembles given the correct chemical conditions described in their article [52]. The crystalline framework assembles because the modified ferritins have coordination complexes (a central metallic ion that surrounding molecules can bind to) that serve as binding sites for Zn²⁺ ions. An organic linker connects Zn²⁺ ion sites between neighboring proteins, creating a node in the larger three-dimensional, porous, crystalline framework.

Non-native quantum dots have not been incorporated into this framework yet. Future work for our group could involve, first, synthesizing non-native cores into these modified ferritins, and second, assembling them to form crystalline frameworks. Our lab has obtained a sample of this modified ferritin from Tezcan's group at UC San Diego. A critical first step in creating such a material is to synthesize high-quality nanocrystal-ferritin constructs using the modified ferritin. I recommend PbS as a starting point since it's likely the most robust synthesis completed in our lab; it appears to work across a wide range of chemical and thermal conditions. After high-quality, uniform PbS-FTN is made, it's possible they will self-assemble under the same conditions used by Sontz, et al.

This framework provides seemingly endless engineering opportunities for anywhere a high packing density of quantum dots is favorable. Perhaps such a framework could be used to build

¹For more information on using HRTEM to image quantum dots adsorbed to mesoporous substrates, I recommend Lidong Sun's study on PbS quantum dots and Ze-Da Meng's study on CdSe quantum dots [50,51].

a p-n junction thin film solar cell, with n-type and p-type quantum dots on opposing sides of the junction. It seems likely the ferritin is too resistive, or will interfere with the sensitive balance between the number of electrons and holes, and ultimately prevent the creation of depletion zone at the junction. The plausibility of such a device could perhaps be determined by collaborating with a BYU professor that does materials simulations. A DSSC approach, where an electrolyte solution added and the protein scaffolding is used to replace TiO_2 , might prove to be a more feasible cell design. Nevertheless, as stated before, incorporation of non-native quantum dots into this framework would be novel regardless of the strength and durability of the bonds. Such a structure would essentially be an artificial solid scaled in size by a factor of ~ 100 , with quantum dots mimicking absorption and emission properties of individual atoms, but bonded together in a very different way. Applications outside photovoltaics, such as manipulable LED structures, seem more likely.

Appendix A

Appendix: Watt Lab Experimental Procedures

Here we include several step-by-step procedures for several common experiments in Dr. Richard Watt's laboratory. The Lowry and Bradford protein assays are not included in this appendix because there are laminated instructions for these assays in Dr. Watt's laboratory.

We begin by making some general remarks about using Dr. Watt's laboratory in room C254 BNSN. Milli-Q water is stored in a white tank above the flammables cabinet and can be refilled in Dr. Anderson's laboratory room (E-270). All flammable solutions including several acids are stored in the yellow flammables cabinet. Non-flammable acids are stored in cabinet H-24. Powders and solid materials are stored by alphabetical order in the glass cabinets. There are special waste containers for glass, aqueous waste, and needles/sharp objects—be sure to check the labels on waste containers to make sure materials are properly disposed of. Do not leave machines running unless they are in use, especially the spectrophotometer and Eppendorf centrifuge. Wash dishes in the sink on the south wall of room C254 using dH₂O from the thin faucet and detergent powder. Allow dishes to dry either on the rack directly above the sink or on a dry paper towel next to the

sink. Return dishes to their storage location after they have dried.

Pipette tips, 1.5 mL vials, 15 mL vials, and 50 mL vials are stored in drawers F-13, F-17, F-22, and F-21 respectively. When stock is low for these items, purchase replacements at BYU's Chemistry Central Stockroom. Other items that often need to be purchased include: 2 μm PES filters and plastic tubing for ICP-MS, septum + aluminum caps, needles, syringes, and latex gloves.

When using the pH meter, be certain to rinse the pH rod in-between samples with dH_2O and dry it with a Kimwipe without touching the bulb at the bottom of the rod. The pH meter should be recalibrated if a sensitive pH measurement is needed. To calibrate the pH meter, first press the "cal" button and wait for the "7" light to start blinking. Submerge the pH bulb in the pH 7 standard solution (usually stored in a 15 mL vial next to the pH meter), wait for the meter to display a stable number, then press the "=" button—the "4/10" light should start blinking to indicate the meter is ready for its second calibrated point. Use the standard buffers to calibrate to pH 4 if measuring the pH of an acidic solution and pH 10 if measuring a basic solution. After pressing "=" to calibrate the second point, the display often needs to be refreshed. To refresh the display, press "Mode" to toggle through "mV", " $^{\circ}\text{C}$ ", and back to "pH". The bulb should always be suspended in the solution for its storage, fully submerged but not touching the bottom of the beaker.

A.1 Apoferritin Preparation

Apoferritin preparation consists of six 8-hour cycles: three cycles of thioglycolic acid and three cycles of sodium bicarbonate. Allowing any cycle to go over 8 hours will not hurt the ferritin.

1. Hydrate the dialysis cassette by letting it soak in dH_2O .
 - The 7000 molecular weight cut off 0.5 - 3.0 mL dialysis cassette from Cole-Parmer is stored in drawer G-12.

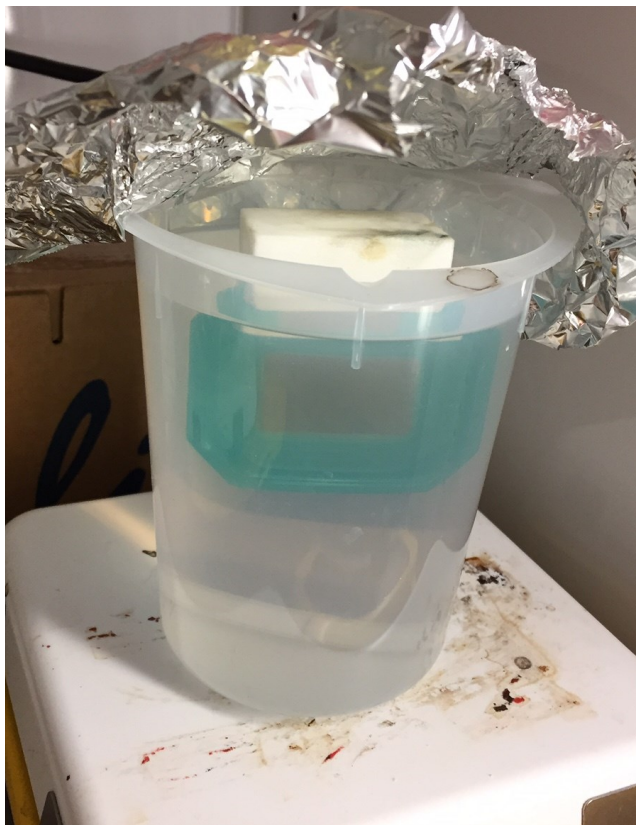


Figure A.1 Ferritin on last cycle of thioglycolic acid dialysis. The solution turns progressively less purple each cycle, indicating fewer iron ions remain within the ferritin. Sometimes the third cycle is still purple, which means a fourth cycle is necessary.

- The foam buoy that allows the cassette to float on the solution's surface is stored in drawer J-23.
2. Use a 3 mL or 5 mL syringe and needle to inject 3 mL of ferritin into the hole "1" on the top corner of the cassette. Be careful not to puncture the membrane.
 3. Fill beaker to 1 L with dH₂O + 7.54 mL thioglycolic acid + 34.02 g sodium acetate.
 4. Use a foam buoy to float the dialysis cassette in beaker, insert stir bar, cover the top with tinfoil to confine the smell, and allow to gently mix in the refrigerator for 8 hours.
- The punctured hole "1" should be above the surface of the water.

- Make sure that the tinfoil doesn't block the cassette from spinning around.
 - The solution should turn purple after several minutes.
5. Dispose of solution by pouring in the container labeled "aqueous waste" (stored underneath the glove box). Return to step 3 and repeat two more 8-hour cycles.
 6. Fill beaker to 1 L with dH₂O + 5 g sodium bicarbonate (NaHCO₃), insert cassette, let mix for 8 hours.
 7. Dispose of the solution down the normal drain. Return to step 6 and repeat two more 8-hour cycles.
 8. Use a 3 or 5 mL syringe and needle to extract the apoferritin out of hole "1".

A.2 Gel Filtration

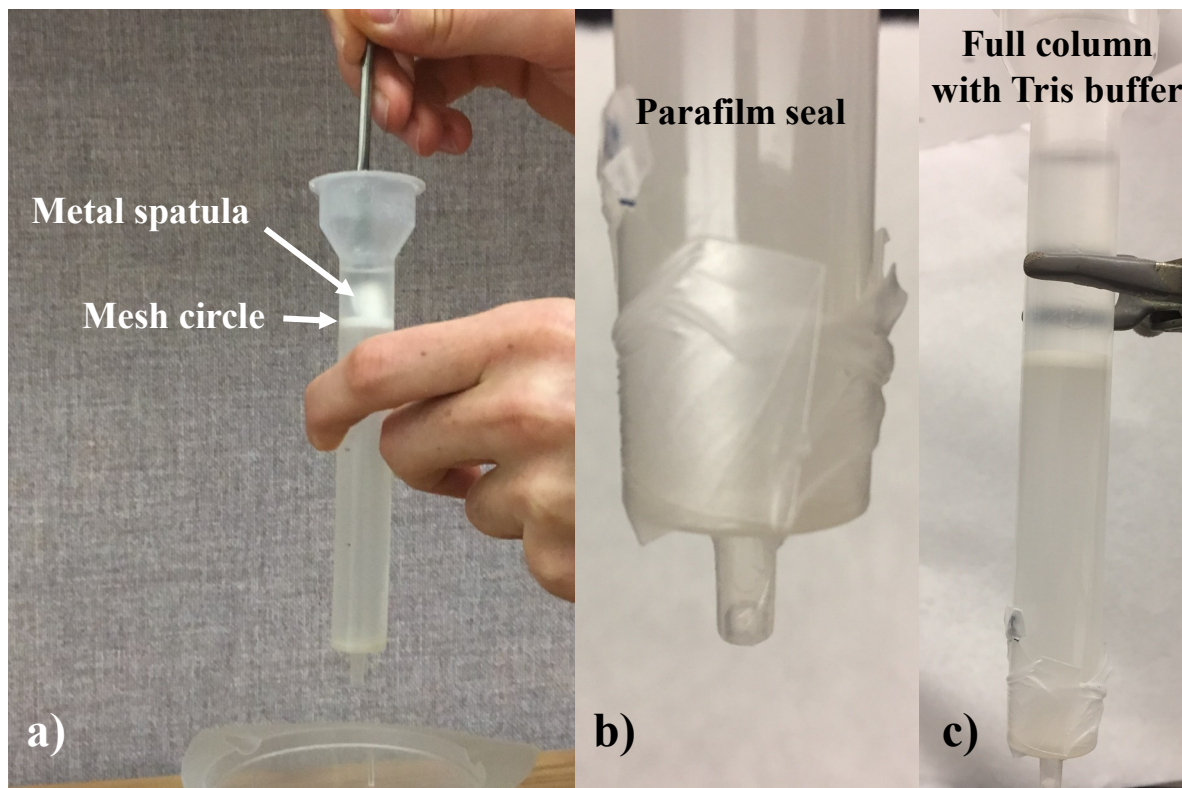


Figure A.2 a) After the gel has solidified at 4°C, a metal spatula or tweezers can be used to push the mesh circle onto and parallel to the gel-water boundary. b) A parafilm seal is used to prevent liquid from passing through the sample. This is necessary for storing the column and when allowing a gel to solidify. c) A complete column stored with Tris buffer on the top to prevent the gel from drying and cracking. An ideal gel is 15 ± 3 mL; this gel, at 12 mL, is on the smaller end.

A.2.1 Making the column

1. Mix 1.1 g Sephadex G-100 with ~ 30 mL of dH₂O (or whichever bead size fits your purposes best, G-100 works well for isolating nanocrystal-ferritin composites).
2. Place beaker in fridge and let it sit for 30 min or longer.

- After 30 min, the gel will sink to the bottom of the beaker. Holding the beaker up against a light source, you should be able to see a boundary between the gel and water.
3. Insert a mesh circle into the bottom of the column, and seal the end with parafilm as seen in Figure A.3 (b).
 4. Pour the water layer into the sink, then pour the gel layer into a 20 mL column, and let the gel resettle for 2 hours or longer.
 - Another gel-water boundary will form, hopefully this boundary near the 15 ± 3 mL mark.
 5. Remove the parafilm cap and insert a second mesh circle in-between the gel and water as seen in Figure A.3 (a).
 - It helps if the circle enters the column perpendicular to the gel-water boundary so it can be easily pushed down. Once close to the boundary, rotate the circle so it separates the gel-water boundary, then press down gently to make sure no water is underneath the sample. There are likely other equally effective ways to achieve the same result, creativity is encouraged.
 6. Pour off excess water, remove the parafilm cap and let $\sim 5 - 10$ mL of Tris pass through the gel.

A.2.2 Running the column

1. Pour out any Tris above the gel and place the column above the first 1 mL vial.
2. Insert 0.5 - 2.5 mL of sample above the top mesh circle, let the sample run past the mesh circle.

3. Add 1 mL Tris buffer and let it run past the mesh grid.
4. Pour Tris into the column until it's topped off.
5. Collect the drips in 1 mL fractions starting from when the sample was first inserted.

A.3 ICP-MS Sample Preparation

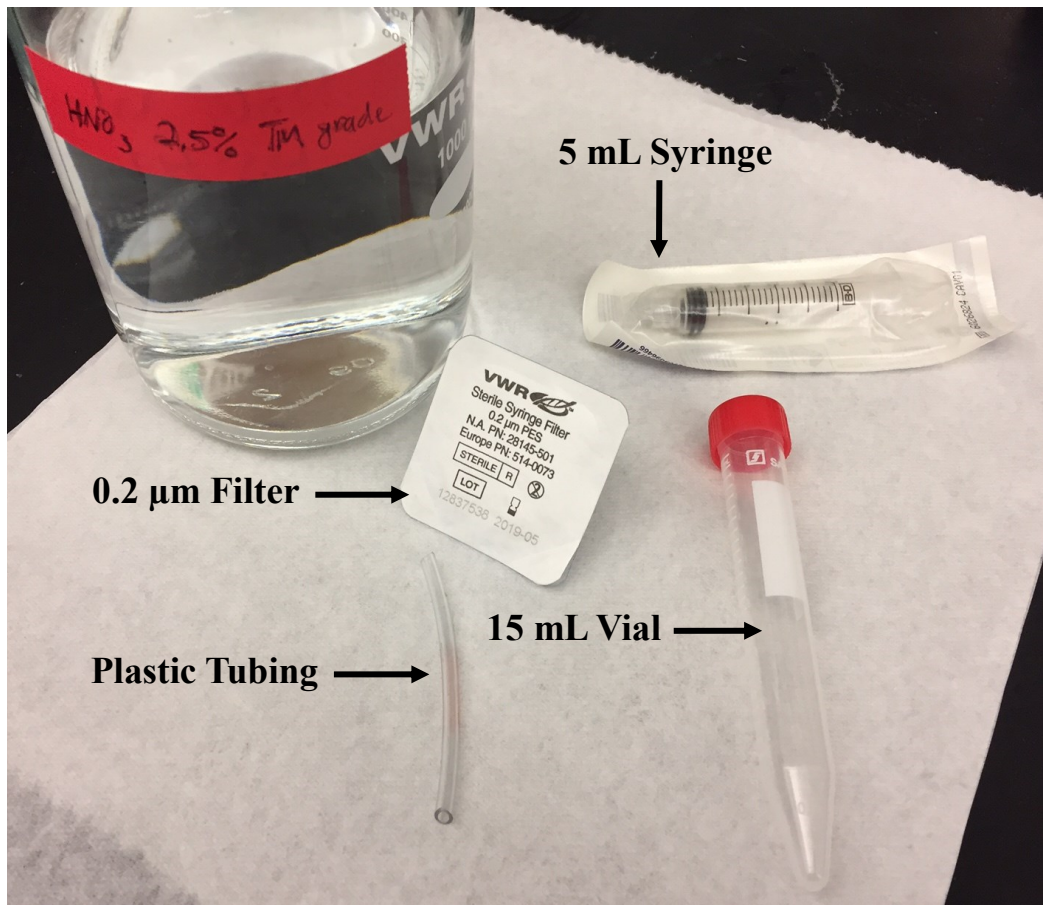


Figure A.3 List of materials for ICP-MS sample preparation.

A.3.1 Materials

1. 2.5 % trace metal grade nitric acid (HNO₃) (on shelf)
2. Plastic tubing cut into 2 - 3 inch segments (drawer H-11).
3. 5 mL syringes (drawer H-14)
4. 2 μL filtration caps (drawer H-11)

5. 15 mL vials, 4 per sample (drawer F-17)

A.3.2 Procedure

1. Prepare 5 standards of 1000, 200, 150, 100, 50, 0 ppb of the metal you wish to measure.
 - Recall $1 \text{ ppb} = 10^{-6} \text{ g/L}$. Metals will be dissolved into 5 mL of HNO_3 , so 1000 ppb for this volume = $5 \times 10^{-6} \text{ g}$ of metal.
 - Since measuring $5 \times 10^{-6} \text{ g}$ of metal accurately can be difficult, I recommend first making $\sim 10 \text{ mM}$ solution, then using this solution to make a $\sim 0.1 \text{ mM}$ solution, then pipetting the correct amount. This is called "serial dilution".
 - Inject metal into 5 mL of HNO_3 to yield 1000, 200, 150, 100, 50, 0 ppb standards. Shake by hand and let sit overnight.
2. Prepare samples
 - Prepare 2 ICP samples for each sample you wish to measure the metal atom concentration of. Inject $20 \mu\text{L}$ and $30 \mu\text{L}$ of gel-filtered sample into 5 mL HNO_3 .
 - Shake samples by hand.
 - Let sit overnight.
 - Centrifuge at 4000 rpm for 5 min.
 - Push a segment of plastic tubing onto the syringe tip, draw in supernatant, and then remove the plastic tubing.
 - Screw a $2 \mu\text{m}$ PES filter onto the syringe, and push the sample out through the filter into a new 15 mL vial.

- Email ICP-MS machine operator to inform him/her the metal atom concentration you wish to measure, your chemistry affiliation (Dr. Richard Watt), and the date you'd like to receive the results by.
- Drop samples off in C295. A key for C295 room is stored in a white box on the windowsill counter of C254.

A.4 TEM Sample Preparation

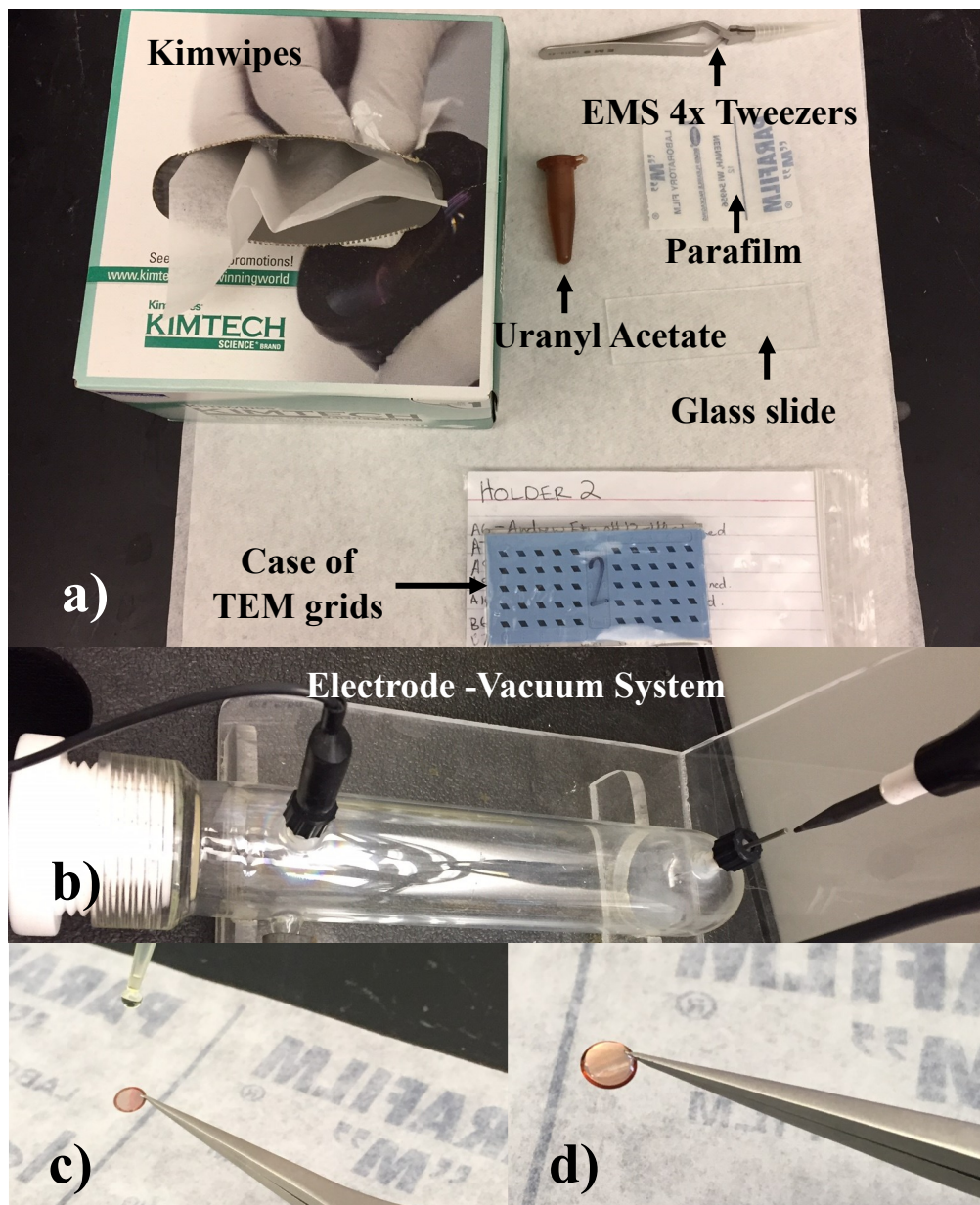


Figure A.4 a) List of materials. b) Electrode vacuum system. c) A 3.5 μL droplet of sample about to be gently placed on TEM grid's dark, copper side. d) A droplet of sample suspended on the TEM grid.

A.4.1 Materials

1. EMS 4X tweezers (drawer E-1)
2. Glass slide (drawer H-13)
3. Parafilm (above flammables cabinet)
4. Uranyl acetate (top right shelf of the glass door refrigerator)
5. Carbon mesh TEM grid (drawer H-13)
6. Kimwipes (above flammables cabinet)

A.4.2 Procedure

1. Remove TEM grid(s) from blue box with tweezers, place on glass slide, insert into the glass chamber of the electrode-vacuum system displayed in Figure A.5 (b). Screw on the air-tight cap.
 - Make sure an O-ring is fastened to the inside of the cap before screwing it on.
2. Turn on the vacuum (black switch on cord), let it pump down for ~ 2 min, then close the vacuum valve and leave the vacuum running.
3. Slowly open the cap to prevent air from rushing in. Remove glass slide without touching the grid(s).
4. Mount a grid on EMS 4X tweezers as seen in Figure A.5(c), with the dark carbon mesh side facing up. Place a $3.5 \mu\text{L}$ droplet of sample onto the grid as seen in Figure A.5 (d). Let sit for 1 min.

5. Rinse the grid in a large dH₂O droplet for one second, use the parafilm as a surface to form the water droplet.
6. Within 2 - 5 seconds of rinsing the grid, gently touch a folded Kimwipe to the edge of the grid. Excess water from all surfaces on the grid will immediately be absorbed by the Kimwipe.
7. If staining is needed, apply a 3.5 μ L droplet of uranyl acetate to the same surface, and repeat the rinsing and drying steps.
 - Uranyl acetate is a negative stain binds to the ferritin shell and is useful for imaging in STEM mode.
 - The uranyl acetate can be stored for >1 year at 4°C. If the solution appears to have crystallized, it can be replaced by a 3 % solution stored in a 15 mL vial that is wrapped in tin-foil and labeled "uranyl acetate" in the same fridge. Dilute the solution to 1.5 % and filter through a 0.2 μ m filter that has been pre-rinsed several times with Milli-Q water.
 - BYU EM specialist Mike Standing can be contacted if uranyl acetate powder is needed.

A.5 Inert Atmospheres

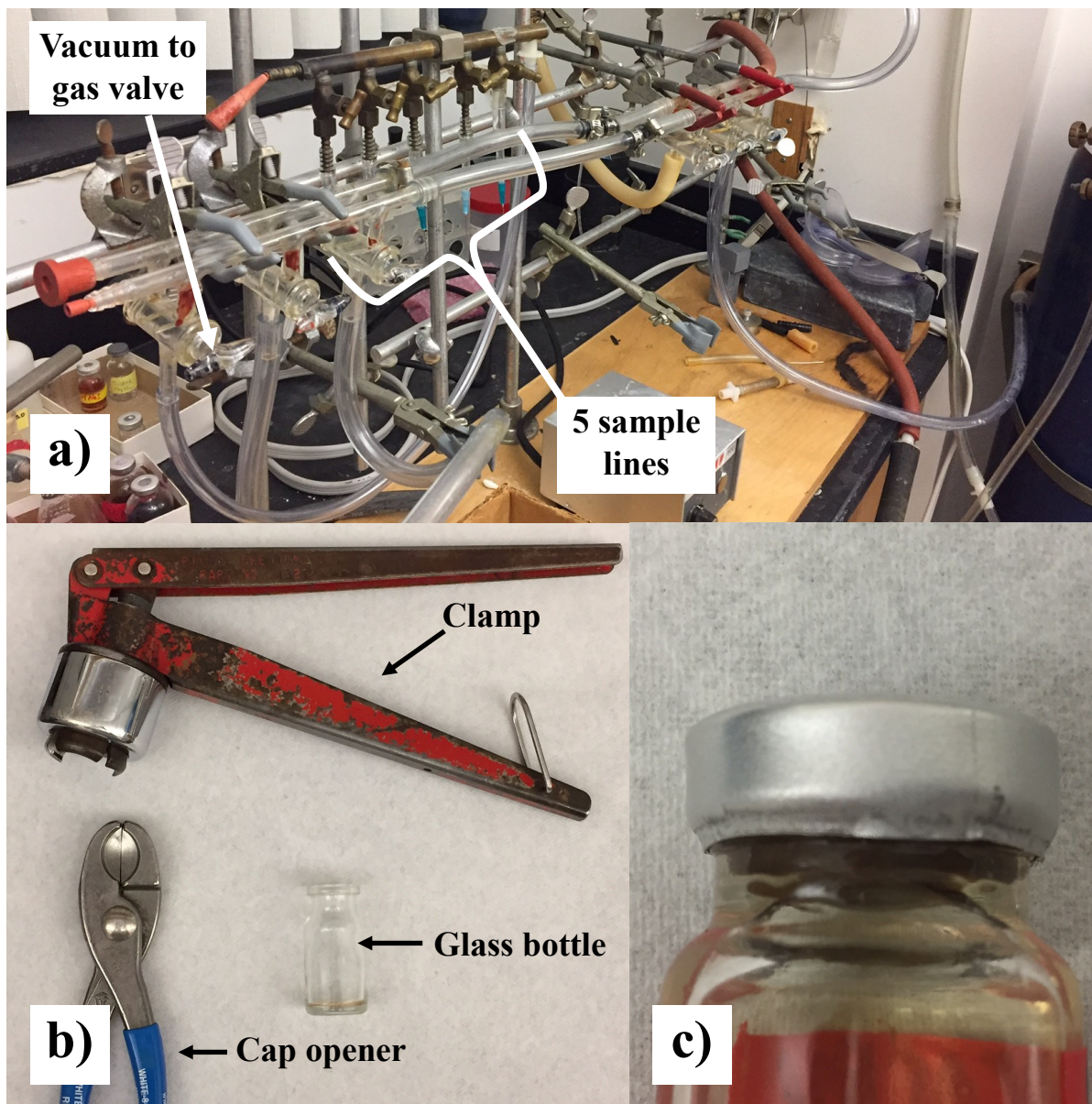


Figure A.5 a) Vacuum-gas manifold system in room C254A. The septum cap is pushed upwards into the needles hanging below the five sample lines and suspended by friction while the vacuum/gas cycles are performed. b) List of materials. c) An example of a septum-aluminum cap tightly clamped on a glass bottle.

There are two options for performing anaerobic experiments: the glove box and the vacuum-gas manifold system. The glove box has the benefit of size—it is large enough for entire experiments to be performed inside. The benefit of the vacuum-gas manifold system lies in its ability to remove more oxygen from liquid samples than the glove box.

A.5.1 Glove Box

The entire glove box is full of nitrogen at a pressure slightly above 1 atm. Transferring items in and out of the glove box requires the use of an intermediate chamber. Follow the instructions taped on the intermediate chamber to do so.

A.5.2 Vacuum-Gas Manifold System

This system allows you to simultaneously create inert atmospheres in 1 - 5 separate bottles.

1. Seal the solution(s) in glass bottle(s) using a septum cap surrounded by an aluminum casing.
 - Turn the septum upside down so the lighter part is facing up.
 - Use the clamp to first press the cap firmly against the top of the glass bottle, and only then squeeze the clamp's handles together. The clamp only pinches $\frac{3}{4}$ of the cap, so rotate 90° and squeeze again. Rotate and squeeze while pressing down on the glass bottle a few more times to get a thorough seal.
 - Septum + aluminum caps are stored in drawer H-28.
 - The clamp and opener for these bottle caps are in drawer K-8.
2. Push the bottle(s) onto any of the five open needles in the vacuum-gas manifold system in room C254A.

3. Open bronze valves above samples, turn on the vacuum pump, twist the glass valve on the far left to the connect vacuum line to the samples.
 - Make sure the valves above any open needles are closed.
 - The amount of air being sucked by the vacuum pump is proportional to the volume of the vacuum pump's gurgling noise.

4. To achieve an inert atmosphere repeat these steps 3 times:
 - Twist glass valve to pump down for 3 minutes.
 - Twist glass valve to fill with argon for 45 seconds.

Bibliography

- [1] B. Hennequin, L. Turyanska, T. Ben, A. M. Beltron, S. I. Molina, M. Li, S. Mann, A. Patan, and N. R. Thomas, “Aqueous near-infrared fluorescent composites based on apoferritin- encapsulated PbS quantum dots,” *Advanced Materials* **20**, 3592–3596 (2008).
- [2] C. Cao *et al.*, “Targeted in vivo imaging of microscopic tumors with ferritin-based nanoprobe across biological barriers,” *Advanced Materials* **26**, 2566–2571 (2014).
- [3] M. Uchida *et al.*, “Targeting of cancer cells with ferrimagnetic ferritin cage nanoparticles,” *Small* **312**, 16626–16633 (2006).
- [4] “\$1/W photovoltaic systems,” Technical report, U.S. Department of Energy (2010) .
- [5] C. Honeyman, “U.S. Residential Solar Economic Outlook 2016-2020: Grid Parity, Rate Design and Net Metering Risk,” Technical report, Green Tech Media (2016) .
- [6] M. Saliba *et al.*, “Incorporation of rubidium cations into perovskite solar cells improves photovoltaic performance,” *Science* (2016).
- [7] L. Turyanska, T. D. Bradshaw, J. Sharpe, M. Li, S. Mann, N. R. Thomas, and A. Patanè, “The biocompatibility of apoferritin-encapsulated PbS quantum dots,” *Small* **5**, 1738–1741 (2009).

- [8] J. S. Wang, H. E. Smith, and G. J. Brown, “Stability and aging studies of lead sulfide quantum dot films: Photoabsorption, morphology, and chemical state characteristics,” *Materials Chemistry and Physics* **154**, 44 – 52 (2015).
- [9] L. Turyanska, O. Makarovskiy, U. Elfurawi, A. Patanè, M. W. Fay, J. W. Bowers, and H. M. Upadhyaya, “Imaging the photovoltaic response of PbS-sensitized porous titania,” *Physica Status Solidi (A) Applications and Materials Science* **208**, 2450–2453 (2011).
- [10] M. Kim, Y. Rho, K. S. Jin, B. Ahn, S. Jung, H. Kim, and M. Ree, “PH-dependent structures of ferritin and apoferritin in solution: Disassembly and reassembly,” *Biomacromolecules* **12**, 1629–1640 (2011).
- [11] J. D. Keyes, R. J. Hilton, J. Farrer, and R. K. Watt, “Ferritin as a photocatalyst and scaffold for gold nanoparticle synthesis,” *Journal of Nanoparticle Research* **13**, 2563–2575 (2011).
- [12] J. Polanams, A. D. Ray, and R. K. Watt, “Nanophase Iron Phosphate, Iron Arsenate, Iron Vanadate, and Iron Molybdate minerals synthesized within the protein cage of ferritin,” *Inorganic Chemistry* **44**, 3203–3209 (2005), PMID: 15847428.
- [13] M. Tominaga, A. Ohira, Y. Yamaguchi, and M. Kunitake, “Electrochemical, {AFM} and {QCM} studies on ferritin immobilized onto a self-assembled monolayer-modified gold electrode,” *Journal of Electroanalytical Chemistry* **566**, 323 – 329 (2004).
- [14] R. Casiday and R. Frey, “Iron use and storage in the body: Ferritin and Molecular Representations,” 1999.
- [15] T. Douglas and V. T. Stark, “Nanophase cobalt oxyhydroxide mineral synthesized within the protein cage of ferritin,” *Inorganic Chemistry* **39**, 1828–1830 (2000).
- [16] P. Arosio, T. G. Adelman, and J. W. Drysdale, “On ferritin heterogeneity. Further evidence for heteropolymers,” *Journal of Biological Chemistry* **253**, 4451 (1978).

- [17] T. Takahashi and S. Kuyucak, “Functional properties of threefold and fourfold channels in ferritin deduced from electrostatic calculations,” *Biophysical Journal* **84**, 2256–2263 (2003).
- [18] J. D. López-Castro, J. J. Delgado, J. a. Perez-Omil, N. Gálvez, R. Cuesta, R. K. Watt, and J. M. Domínguez-Vera, “A new approach to the ferritin iron core growth: influence of the H/L ratio on the core shape,” *Dalton Transactions* **41**, 1320 (2012).
- [19] N. E. L. Brun, A. Crow, M. E. Murphy, A. G. Mauk, and G. R. Moore, “Iron core mineralisation in prokaryotic ferritins,” *Biochimica et Biophysica Acta (BBA) - General Subjects* **1800**, 732 – 744 (2010).
- [20] S. D. Erickson, T. J. Smith, L. M. Moses, R. K. Watt, and J. S. Colton, “Non-native Co-, Mn-, and Ti-oxyhydroxide nanocrystals in ferritin for high efficiency solar energy conversion,” *Nanotechnology* **26**, 015703 (2015).
- [21] R. K. Watt, O. D. Petrucci, and T. Smith, “Ferritin as a model for developing 3rd generation nano architecture organic/inorganic hybrid photo catalysts for energy conversion,” *Catal. Sci. Technol.* **3**, 3103–3110 (2013).
- [22] L. Turyanska, T. D. Bradshaw, J. Sharpe, M. Li, S. Mann, N. R. Thomas, and A. Ál, “The biocompatibility of apoferritin-encapsulated PbS quantum dots,” *Small* **5**, 1738–1741 (2009).
- [23] C. R. Olsen *et al.*, “Permanganate-based synthesis of manganese oxide nanoparticles in ferritin,” *Nanotechnology* **28**, 195601 (2017).
- [24] T. Douglas and D. R. Ripoll, “Calculated electrostatic gradients in recombinant human H-chain ferritin,” *Protein Science: a publication of the Protein Society* **7**, 1083–1091 (1998).
- [25] J.-W. Lee, D.-Y. Son, T. K. Ahn, H.-W. Shin, I. Y. Kim, S.-J. Hwang, M. J. Ko, S. Sul, H. Han, and N.-G. Park, “Quantum-dot-sensitized solar cell with unprecedentedly high photocurrent,” *Scientific Reports* **3**, 1050 (2013).

- [26] W. Shockley and H. J. Queisser, "Detailed balance limit of efficiency of p-n junction solar cells," *Journal of Applied Physics* **32**, 510–519 (1961).
- [27] R. J. Ellingson, M. C. Beard, J. C. Johnson, P. Yu, O. I. Micic, A. J. Nozik, A. Shabaev, and A. L. Efros, "Highly efficient multiple exciton generation in colloidal PbSe and PbS quantum dots," *Nano Letters* **5**, 865–871 (2005), PMID: 15884885.
- [28] M. C. Beard, A. G. Midgett, M. Law, O. E. Semonin, R. J. Ellingson, and A. J. Nozik, "Variations in the quantum efficiency of multiple exciton generation for a series of chemically treated PbSe nanocrystal films," *Nano Letters* **9**, 836–845 (2009).
- [29] G. L. Peterson, "A simplification of the protein assay method of Lowry et al. which is more generally applicable," *Analytical Biochemistry* **83**, 346–356 (1977).
- [30] T. D. Bradshaw, M. Junor, A. Patanè, P. Clarke, N. R. Thomas, M. Li, S. Mann, and L. Turyanska, "Apoferitin-encapsulated PbS quantum dots significantly inhibit growth of colorectal carcinoma cells," *Journal of Materials Chemistry B* **1**, 6254 (2013).
- [31] L. Bakueva, I. Gorelikov, S. Musikhin, X. S. Zhao, E. H. Sargent, and E. Kumacheva, "PbS quantum dots with stable efficient luminescence in the near-IR spectral range," *Advanced Materials* **16**, 926–929 (2004).
- [32] N. S. Arul and V. D. Nithya, "Molybdenum disulfide quantum dots: synthesis and applications," *RSC Adv.* **6**, 65670–65682 (2016).
- [33] Y. Wang and Y. Ni, "Molybdenum disulfide quantum dots as a photoluminescence sensing platform for 2,4,6-trinitrophenol detection," *Analytical Chemistry* **86**, 7463–7470 (2014), PMID: 25001878.

- [34] M. M. Bradford, "A rapid and sensitive method for the quantitation of microgram quantities of protein utilizing the principle of protein-dye binding," *Analytical Biochemistry* **72**, 248–254 (1976).
- [35] O. H. Lowry *et al.*, "Protein measurement with the Folin phenol reagent," *J Biol Chem* **193**, 265–275 (1951).
- [36] B.-G. Han, R. W. Walton, A. Song, P. Hwu, M. T. Stubbs, S. M. Yannone, P. Arbel-Åez, M. Dong, and R. M. Glaeser, "Electron microscopy of biotinylated protein complexes bound to streptavidin monolayer crystals," *Journal of Structural Biology* **180**, 249 – 253 (2012).
- [37] R. Plass, S. Pelet, J. Krueger, M. Grätzel, and U. Bach, "Quantum dot sensitization of organic-inorganic hybrid solar cells," *The Journal of Physical Chemistry B* **106**, 7578–7580 (2002).
- [38] Y. Yang, W. Rodríguez-Córdoba, X. Xiang, and T. Lian, "Strong electronic coupling and ultrafast electron transfer between PbS quantum dots and TiO₂ nanocrystalline films," *Nano Letters* **12**, 303–9 (2012).
- [39] Y. Nicolau, "Solution deposition of thin solid compound films by a successive ionic-layer adsorption and reaction process," *Applications of Surface Science* **22-23**, 1061–1074 (1985).
- [40] H. Lee *et al.*, "PbS and CdS quantum dot-sensitized solid-state solar cells: "Old concepts, new results"," *Advanced Functional Materials* **19**, 2735–2742 (2009).
- [41] X. Song, M. Wang, H. Zhang, J. Deng, Z. Yang, C. Ran, and X. Yao, "Morphologically controlled electrodeposition of CdSe on mesoporous TiO₂ film for quantum dot-sensitized solar cells," *Electrochimica Acta* **108**, 449–457 (2013).
- [42] D. Martineau, "The assembly guide for making your own solar cells," *Solaronix* pp. 3–38 (2012).

- [43] “Standard Tables for References Solar Spectral Irradiance at Air Mass 1.5: Direct Normal and Hemispherical for a 37 Degree Tilted Surface,” 1998.
- [44] C. R. Olsen, J. S. Embley, K. R. Hansen, A. M. Henrichsen, J. R. Peterson, J. S. Colton, and R. K. Watt, “Tuning Ferritin’s band gap through mixed metal oxide nanoparticle formation,” *Nanotechnology* **28**, 195604 (2017).
- [45] J. Wall, J. Langmore, M. Isaacson, and A. V. Crewe, “Scanning transmission electron microscopy at high resolution,” *Proceedings of the National Academy of Sciences of the United States of America* **71**, 1–5 (1974).
- [46] G. Calogero, J. H. Yum, A. Sinopoli, G. Di Marco, M. Grätzel, and M. K. Nazeeruddin, “Anthocyanins and betalains as light-harvesting pigments for dye-sensitized solar cells,” *Solar Energy* **86**, 1563–1575 (2012).
- [47] C. Y. Chien and B. D. Hsu, “Optimization of the dye-sensitized solar cell with anthocyanin as photosensitizer,” *Solar Energy* **98**, 203–211 (2013).
- [48] N. J. Cherepy, G. P. Smestad, M. Gratzel, and J. Z. Zhang, “Ultrafast electron injection: Implications for a photoelectrochemical cell utilizing an anthocyanin dye-sensitized TiO₂ nanocrystalline electrode,” *Journal of Physical Chemistry B* **101**, 9342–9351 (1997).
- [49] J. O. Ozuomba, L. U. Okoli, A. J. Ekpunobi, and F. Science, “The performance and stability of anthocyanin local dye as a photosensitizer for DSSCs,” *Advances in Applied Science Research* **4**, 60–69 (2013).
- [50] L. Sun, Z. Y. Koh, and Q. Wang, “PbS quantum dots embedded in a ZnS dielectric matrix for bulk heterojunction solar cell applications,” *Advanced Materials* **25**, 4598–4604 (2013).

-
- [51] Z.-D. Meng, L. Zhu, S. Ye, Q. Sun, K. Ullah, K.-Y. Cho, and W.-C. Oh, “Fullerene modification CdSe/TiO₂ and modification of photocatalytic activity under visible light,” *Nanoscale Research Letters* **8**, 1–10 (2013).
- [52] P. A. Sontz, J. B. Bailey, S. Ahn, and F. A. Tezcan, “A metal organic framework with spherical protein nodes: rational chemical design of 3D protein crystals,” *Journal of the American Chemical Society* **137**, 11598–11601 (2015), pMID: 26305584.